

From crustal thickening to orogen-parallel escape: the 120 Ma-long HT-LP evolution of the Paleozoic Famatinian back-arc, NW Argentina

Pablo Guillermo Farias^{1,1}, Roberto F. Weinberg^{1,1}, Alfonso Sola^{2,2}, and Raúl Becchio^{3,3}

¹Monash University

²Universidad de Salta. IBIGEO-CONICET

³INENCO-CONICET

November 30, 2022

Abstract

Exposed sections of accretionary orogens allow reconstruction of their tectonic evolution. Most commonly, orogens are characterised by two-dimensional shortening perpendicular to the orogenic front. We describe the mid-crustal section of the back-arc of the early Paleozoic Famatinian accretionary orogen, exposed in the Sierra de Quilmes. Here crustal deformation evolved from a typical two-dimensional shortening with tectonic transport towards the west, to a non-coaxial constrictional strain with a southward tectonic transport parallel to the orogen. During the early phase of deformation, HT-LP metamorphic complexes were juxtaposed by west-directed thrusting on remarkably thick shear zones forming a thrust duplex. Deformation of the buried footwall complex continued after the exhumed hanging wall ceased to deform. We suggest that the thermally-weakened footwall complex responded by initiating a phase of south-verging thrusting, parallel to the orogen, associated with strong constriction, associated with L-tectonites, and sheath folds. This late phase of deformation defines a non-coaxial constrictional regime characterized by simultaneous east-west and vertical shortening and strong north-south, orogen-parallel stretching. Titanite ages and Zr-in-titanite thermometry demonstrate that this back-arc remained above 700 °C for 120 Ma between 500 and 380 Ma. Combined with regional geology, the new data suggest that west-verging thrusting interrupted an early, back-arc extensional phase, and lasted from ~ 470 to 440 Ma, and that footwall constriction and south-verging thrusting continued for another 40 to 60 Ma. The Famatinian back-arc exposed in Sierra de Quilmes thus is an example of how shortening and orogenic growth in a hot orogen was counterbalanced by lateral flow.

1 From crustal thickening to orogen-parallel escape: the 120 Ma-long
2 HT-LP evolution of the Paleozoic Famatinian back-arc, NW Argentina

3 Pablo Farias¹, Roberto F. Weinberg¹, Alfonso Sola³, Raul Becchio^{2,3}.

4 1. School of Earth, Atmosphere and Environment, Monash University, Clayton, Victoria 3800,
5 Australia

6 2. LaTe Andes, Las Morereas 510, Vaqueros, Salta, Argentina

7 3. Instituto Geonorte, Universidad Nacional de Salta, INENCO-CONICET, Av. Bolivia 5150, 4400
8 Salta, Argentina

9 **Keywords:** Accretionary orogeny, Famatinian orogen, HT-LP, long-lived orogen, structural geology,
10 titanite geochronology

11 **Key points:**

12 1-Understanding how crustal thickening in the Famatinian back-arc was counterbalanced by a long-
13 lived orogen-parallel stretching event

14 2-Titanite geochronology and geothermometry suggest that the footwall block remained hot for ~60
15 Myr longer than the hanging wall

16 **Plain language summary:** This paper contributes to the understanding of the structural and
17 thermal evolution of a mountain belt in a tectonic plate margin. Our study case is the Ordovician
18 Famatinian orogen (mountain belt), in NW Argentina. We found that the orogen reacted to both
19 tectonic and gravitational forces by stretching laterally under constriction rather than growing
20 vertically as its foundations were thermally weakened. Geochronology and thermometry from
21 titanite indicate that the core of this orogen was partially molten for ~100 million years, and cooled
22 very slowly. These partially molten rocks undermined the stability of the orogen and ultimately
23 caused its failure and lateral flow.

24 [Abstract](#)

25 Exposed sections of accretionary orogens allow reconstruction of their tectonic evolution. Most
26 commonly, orogens are characterised by two-dimensional shortening perpendicular to the orogenic
27 front. We describe the mid-crustal section of the back-arc of the early Paleozoic Famatinian
28 accretionary orogen, exposed in the Sierra de Quilmes. Here crustal deformation evolved from a
29 typical two-dimensional shortening with tectonic transport towards the west, to a non-coaxial
30 constrictional strain with a southward tectonic transport parallel to the orogen. During the early phase
31 of deformation, HT-LP metamorphic complexes were juxtaposed by west-directed thrusting on
32 remarkably thick shear zones forming a thrust duplex. Deformation of the buried footwall complex
33 continued after the exhumed hanging wall ceased to deform. We suggest that the thermally-weakened
34 footwall complex responded by initiating a phase of south-verging thrusting, parallel to the orogen,
35 associated with strong constriction, associated with L-tectonites, and sheath folds. This late phase of
36 deformation defines a non-coaxial constrictional regime characterized by simultaneous east-west and
37 vertical shortening and strong north-south, orogen-parallel stretching. Titanite ages and Zr-in-titanite
38 thermometry demonstrate that this back-arc remained above 700 °C for 120 Ma between 500 and 380
39 Ma. Combined with regional geology, the new data suggest that west-verging thrusting interrupted an
40 early, back-arc extensional phase, and lasted from ~ 470 to 440 Ma, and that footwall constriction and
41 south-verging thrusting continued for another 40 to 60 Ma. The Famatinian back-arc exposed in
42 Sierra de Quilmes thus is an example of how shortening and orogenic growth in a hot orogen was
43 counterbalanced by lateral flow.

44 1. Introduction

45 Rocks within orogens move through evolving thermal and structural fields (Jamieson and Beaumont,
46 2013). Continental back-arcs in accretionary orogens are characterised by long-lasting high-
47 temperature and low-pressure (HT-LP) metamorphism spread along broad zones (Curie and
48 Hyndman, 2006; Wolfram et al., 2019) due to the thinner lithosphere interacting with the
49 asthenosphere (Heuret et al., 2007; Heuret and Lallemand, 2005; Hyndman et al., 2005). This
50 thermally weakened crustal section is susceptible to deformation in response to subduction dynamics
51 (Curie and Hyndman, 2006; Heuret and Lallemand, 2005; Jamieson and Beaumont, 2013) and can
52 record switches between extension and shortening events (Collins, 2002; Lister and Forster, 2009).
53 Strain in such orogens can be partitioned into pure and simple shear during compression (Braathen et
54 al., 2000; Carreras et al., 2013; Fletcher and Bartley, 1994; Hajná et al., 2012; Malavieille, 1993;
55 Rubio Pascual et al., 2016; Sullivan, 2009; Sullivan and Law, 2007), or extension (Jolivet et al., 2004;
56 Mancktelow and Pavlis, 1994), and sometimes it can be associated with constriction (Jolivet et al.,
57 2004; Sullivan and Law, 2007). More significantly, a number of papers documented tectonic transport
58 directions that deviates from the direction perpendicular to the orogen. For example, (Chardon et al.,
59 2009) reviewed several Precambrian accretionary orogens where sections of the crust flowed parallel
60 to the orogen in response to tectonic shortening. They suggested that this may be analogous to what
61 happens in current, wide hot orogens, like the Cordilleran or Tibetan belts. Numerical modelling of
62 mid-crustal levels led to several scenarios dominated by orogen-parallel flow (Chardon and
63 Jayananda, 2008; Chardon et al., 2011; Parsons et al., 2016).

64 Here we investigate the mid-crustal section of a continental back-arc, part of the early Paleozoic (pre-
65 Andean) Famatinian orogen in the Sierra de Quilmes, NW Argentina (Fig. 1). This orogeny was a
66 long-lived, wide and hot accretionary orogeny, located in the active margin of Western Gondwana
67 and part of the regional Terra Australis orogen (Cawood, 2005). The Famatinian back-arc is
68 associated with wide shear zones that accommodated convergence (Finch et al., 2015; Finch et al.,
69 2017; Larrovere et al., 2016; Larrovere et al., 2008; Semenov et al., 2019). It records ca. 60 million
70 years of magmatism and HT-LP metamorphism, between ~500 and 440 Ma (Büttner et al., 2005;

71 Finch et al., 2017; Ortiz et al., 2019; Sola et al., 2013; Sola et al., 2017; Wolfram et al., 2019). We
72 present new structural and geochronology data that yield insights into processes possibly acting today
73 inside ongoing accretionary orogens like the neighbouring central Andes or the North American
74 Cordillera.

75 Wolfram et al. (2019) determined that the 60 Ma duration of high heat flux in this area possibly
76 occurred as multiple pulses. Weinberg et al. (2018) argued that the Famatinian orogen widened
77 because it was too hot to give rise to a thick crust. Here we focus on the combined questions
78 surrounding the nature of the long-lived high heat flux and the orogenic flow, to understand how the
79 hot back-arc crust responded to continued E-W crustal shortening. This paper starts with a review of
80 the regional geology including the Sierra de Quilmes. This is followed by the methods and a
81 description of the results of several mapping campaigns before detailing the results of titanite U-Pb
82 geochronology and chemistry. We discuss the results in terms of the 3D evolution of the orogen and
83 how it responded to crustal thickening, and use the thermal and temporal constraints provided by
84 titanite to argue that the orogeny remained hot for 120 Ma.

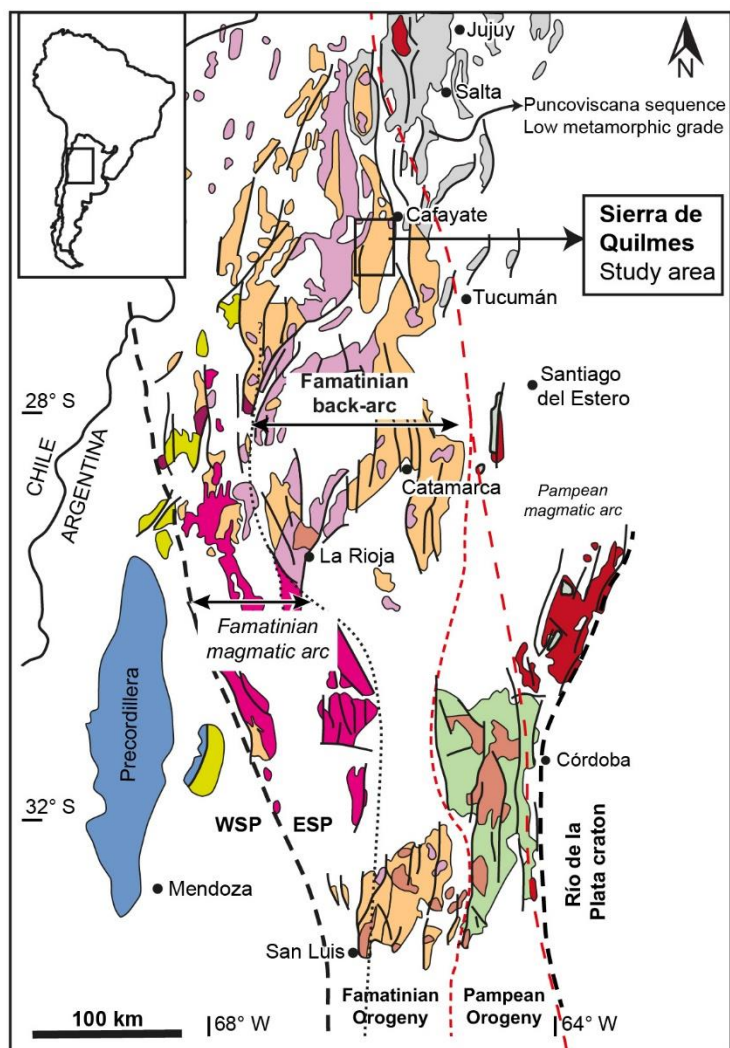
85 2 Regional Geology

86 2.1 Famatinian orogeny in the Sierras Pampeanas

87 The Sierra de Quilmes is part of the Sierras Pampeanas province (Fig. 1), which comprises a number
88 of north-south trending mountain ranges located between 24° and 34°S and 64° and 68°W (Büttner et
89 al., 2005) in the current Andean foreland of west Argentina. These mountains have been part of an
90 accretionary margin developed along West Gondwana during Paleozoic times, as part of the larger
91 Terra Australis orogen (Cawood, 2005; Schwartz et al., 2008). Due to the current flat-slab subduction
92 under the Andes, the Sierras Pampeanas were uplifted exposing different crustal levels (Ramos,
93 2009). The Sierras Pampeanas are composed almost exclusively of Neoproterozoic to Paleozoic meta-
94 sedimentary and igneous rocks shaped during the Pampean (~540-520 Ma), Famatinian (~500-440
95 Ma) and Achaian (~390-350 Ma) orogenies. These orogenies were driven by subduction of the proto-
96 Pacific ocean, and each ended after the accretion of a Laurentian-derived terranes (Aceñolaza et al.,
97 2002; Astini, 1998; Escayola et al., 2011; Omarini et al., 1999; Ramos et al., 1998; Ramos et al.,

98 2000; Ramos et al., 1986; Rapela et al., 1998b; Rapela et al., 2015). Thus, the Famatinian orogenic
99 cycle was a subduction-related Andean-type continental orogeny.

100 The Famatinian orogeny comprised a magmatic arc forming a N-S belt bound to the west by a back-
101 arc, that was extensively migmatized and that today includes the Sierra de Quilmes (Fig. 1). The
102 orogenic cycle initiated at ~505-500 Ma, as indicated by zircon U/Pb ages in peraluminous magmatic
103 rocks of the Famatinian back-arc (Bahlburg et al., 2016; Wolfram et al., 2017). The back-arc was
104 dominated initially by an extensional tectonic regime with the development of marine sedimentary
105 basins between ~485 and 470 Ma (Astini, 2008; Bahlburg and Breitzkreuz, 1991; Bahlburg and Hervé,
106 1997b; Büttner, 2009; Moya, 2015; Rapela et al., 2018). Deformation in the back-arc switched to
107 shortening after ~470 Ma (Weinberg et al., 2018), starting the event known as the Oclóyic phase
108 (Turner, 1975). This event was triggered by the arrival and docking of the Laurentian-derived
109 Precordillera/Cuyania block to the western margin of Gondwana, and marked by regional
110 unconformities formed during the inversion of the basins (Astini and Dávila, 2004; Bahlburg and
111 Hervé, 1997a; Davila et al., 2003; Ramos, 2008; Thomas and Astini, 2003). This phase was
112 characterized by folding and development of several wide thrusts at mid-crustal levels (Finch et al.,
113 2015; Larrovere et al., 2016; Larrovere et al., 2011; Rapela et al., 1998a; Semenov et al., 2019;
114 Semenov and Weinberg, 2017). The Famatinian orogenic cycle is inferred to have finished at around
115 440-435 Ma when magmatism waned (2009; Bahlburg et al., 2016; Büttner et al., 2005; Mulcahy et
116 al., 2014; Wolfram et al., 2017).



- Devonian (Achalian) igneous rocks
- Late Cambrian–Ordovician (Famatinian) S-type igneous rocks
- Late Cambrian–Ordovician (Famatinian) I-type igneous rocks
- Ordovician metamorphic age (medium- to high-grade metasedimentary rocks, Puncoviscana equivalent)
- Early Cambrian (Pampean) igneous rocks
- Cambrian metamorphic age (medium- to high-grade metasedimentary rocks, Puncoviscana equivalent)
- Precordillera terrane
- Puncoviscana sequence
- MARA block (Western Sierras Pampeanas)
- Shear zone
- Faults
- Shear zones

117

118 *Figure 1. Regional map of Sierras Pampeanas. WSP, Western Sierras Pampeanas*
 119 *(Laurentian-derived terranes), ESP, Eastern Sierras Pampeanas (Gondwana-derived*
 120 *terrane). The Sierra de Quilmes is part of the Famatinian back-arc.*

121 2.2 Geology of the Sierra de Quilmes

122 The mid-crustal section of the Famatinian back-arc exposed in Sierra de Quilmes comprises
123 dominantly of the Neoproterozoic to Cambrian turbidite of the Puncoviscana sequence (Adams et al.,
124 2011; Rapela, 1976; Toselli et al., 1978). These rocks record HT-LP Buchan series metamorphism,
125 and reached granulite facies undergoing extensive partial melting that gave rise to vast migmatites and
126 peraluminous granite intrusions (Büttner et al., 2005; Finch et al., 2015). Several workers have
127 studied the northern part of the Sierra de Quilmes (Büttner, 2009; Büttner et al., 2005; Finch et al.,
128 2015; Finch et al., 2016; Rossi and Toselli, 1976; Toselli et al., 1978; Wolfram et al., 2017; Wolfram
129 et al., 2019), leaving the southern part of the range relatively unexplored. Toselli et al. (1978) and
130 Rapela (1976) first divided the area into two complexes that record different metamorphic conditions
131 and were juxtaposed tectonically: the Tolombon and the Agua del Sapo complexes (Fig. 2).

132 2.2.1 *Tolombon complex*

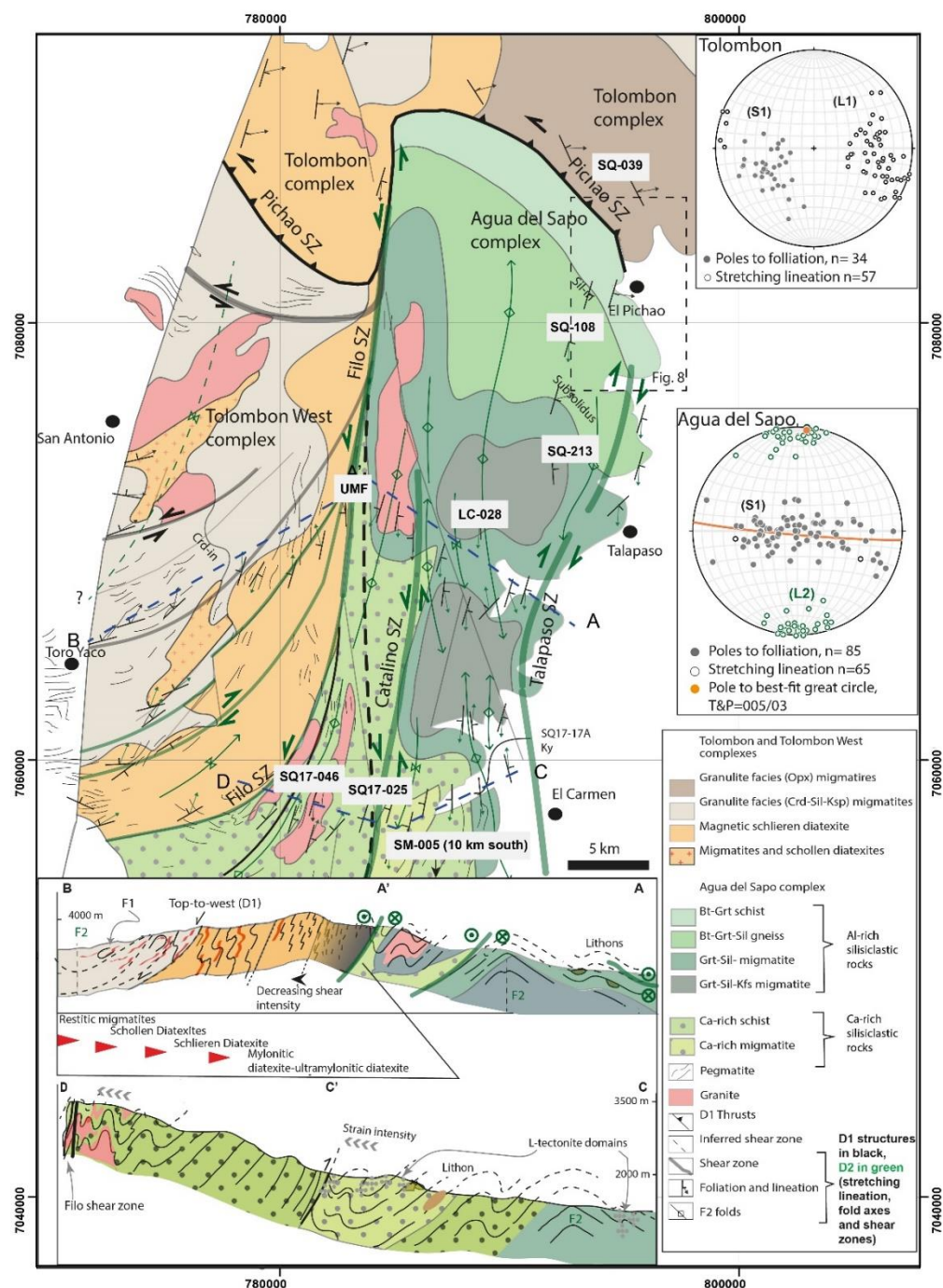
133 The Tolombon complex comprises Al-rich siliciclastic turbidites of the Puncoviscana sequence
134 (Toselli et al., 1978). The metamorphic facies in this complex grades over short distances from
135 greenschist facies chlorite zone in the northeast to granulite facies, garnet-cordierite-sillimanite zone
136 and orthopyroxene zone in the south-west, immediately above the Pichao Shear Zone (Finch et al.,
137 2015). This shear zone thrust this sequence over the Agua del Sapo complex (Fig. 2). The isograds are
138 parallel to the dominant NE-dipping, metamorphic foliation and bedding (Büttner et al., 2005; Finch
139 et al., 2015). The granulite facies rocks underwent extensive partial melting, with peak metamorphic
140 conditions estimated at <6 kbar and 800 °C (Büttner et al., 2005). Migmatites range from metatexite to
141 diatexite, and are the source of leucogranitic peraluminous plutons and different generations of
142 pegmatites that intrude the area (Büttner et al., 2005; Finch et al., 2015; Toselli et al., 1978; Wolfram
143 et al., 2017). The HT-LP anatectic conditions and magmatism of the Tolombon complex lasted for a
144 notably long period of ~60 Ma, between ~505-500 and ~440 Ma, indicated by zircon and monazite U-
145 Pb geochronology (LA-ICPMS and SHRIMP) of migmatites (Finch et al., 2017; Weinberg et al.,
146 2020; Wolfram et al., 2019).

147 The dominant foliation is part of a deformation event that thrusting rocks to the west, as indicated by
148 asymmetric kinematic indicators (Finch et al., 2017). It also defines the axial planar foliation of
149 asymmetric isoclinal west-verging folds (F1) with sub-horizontal fold axes trending roughly north-
150 south. Many F1 folds are intruded by leucosomes along the axial plane, indicative of syn-anatectic
151 folding and thrusting (Finch et al., 2017). F1 folds tighten and shearing intensity increases towards the
152 Pichao Shear Zone.

153 *2.2.2 Pichao Shear Zone and Agua del Sapo complex*

154 The Pichao Shear Zone (PSZ) is 3 km-wide and dips moderately NE (Finch et al., 2015). The strain
155 intensity increases towards the footwall reaching ultramylonites that form a band of up to 1 km thick
156 (Finch et al., 2015). The PSZ is characterised by: (i) microstructural features and mineral paragenesis
157 that constrain deformation to between 500-700 °C variably overprinted by greenschist facies
158 paragenesis; (ii) pervasive top-to-west kinematics recording thrusting of the hanging wall Tolombon
159 complex over the footwall Agua del Sapo complex; and (iii) porphyroclasts and geochemical
160 signature of mylonites indicative of a diatexite migmatite protolith, similar to those of the Tolombon
161 complex (Finch et al., 2015).

162 The Agua del Sapo complex in the footwall of this shear zone is comprised not only by Al-rich
163 turbidites like the hanging wall, but also by Ca-rich turbidites that now form Hbl-Ttn-Aln-Ep- bearing
164 rocks (Toselli et al., 1978). Toselli et al. (1978) noticed that unlike the granulite facies of the hanging
165 wall, the immediate footwall of the shear zone comprises amphibolite facies rocks. Piñán-Llamas and
166 Simpson (2009) investigated the structural makeup of these turbidite-derived metamorphic rocks
167 suggesting that they were only deformed during the Cambrian Pampean orogeny. However, Finch et
168 al. (2017) reported monazite U-Pb ages that range between 435-420 Ma, ~20 Myr younger than
169 monazite ages in the hanging wall. This paper focuses on this poorly-investigated complex and its
170 tectonic boundary to the west.



171

172 *Figure 2. Geological map of the Sierra de Quilmes and its three complexes. Location of*
 173 *titanite samples in labelled grey text box. A-A'-B cross section: dextral and sinistral shear*
 174 *zones and upright folding in the Agua del Sapo complex. C-C'-D cross section: southern*
 175 *section of the Agua del Sapo complex. The strain intensity increases towards the major*
 176 *shear zone in the west recorded by tightening of upright folds.*

177 3 Methods

178 3.1 Aeromagnetic data

179 In order to support field mapping efforts, aeromagnetic data were used to interpret structures and
180 major lithological subdivisions. The aeromagnetic survey, designed by SEGEMAR (the Argentinian
181 Geological Service), was commissioned and completed in July 1998. It comprised N-S flight lines
182 with a 1000 m of separation between lines and tie lines every 7500 m. The total magnetic intensity
183 (TMI) grid after corrections was provided by SEGEMAR. The total magnetic intensity grid was
184 processed here to generate the reduced to the pole grid (RTP; Fig. 3a). From the RTP other images
185 were generated using different filters (Fig. 3).

186 3.2 Crystallographic preferred orientation

187 In order to determine the nature and temperature of quartz deformation, we analysed the
188 crystallographic preferred orientation (CPO) of quartz-rich rocks. The G50 Fabric Analyser at the
189 School of Earth, Atmosphere and Environment, Monash University was used to measure individual
190 quartz grain c-axis orientation in thin section. The c-axes were used to determine the CPO pattern
191 (Paternell et al., 2010; Wilson et al., 2007). The raw data from the Fabric Analyser was processed in
192 the crystal imaging system *INVESTIGATOR G50 v5.9* software to select the c-axis orientation of
193 specific quartz grains within mono-mineralic quartz ribbons or quartz-rich areas. The quality and
194 accuracy of the data were assessed using two factors for every data point: the geometric and
195 retardation quality. The first is a measure of the closeness of the extinction planes from the different
196 light directions, and the second evaluates the usefulness of the c-axis azimuths. Following procedures
197 in Paternell et al. (2010) and Hunter et al. (2016), values of geometric and retardation quality of <75
198 were excluded from the analysis. Equal area stereonet diagrams were created for each sample.

199 3.3 Titanite geochronology

200 U-Pb dating of titanite was carried out at the School of Earth, Atmosphere and Environment, Monash
201 University, by means of laser ablation ICP-MS in a split stream mode (LASS-ICP-MS). Trace
202 elements, and U-Pb isotopes were analysed for every ablation site. U-Pb isotopes were analysed using

203 a Thermo ICP-TQ triple quadrupole ICP-MS coupled with an ASI Resolution 193 nm excimer laser
204 equipped with a dual volume Laurus Technik S155 ablation cell. Titanite was sampled in a He
205 atmosphere with the laser operating at a repetition rate of 10 Hz and a 25 μm spot size. The laser
206 energy used was approximately 4 J cm^{-2} . The ablated material fed the ICPMS torches for the U-Pb
207 analysis. Instrumental mass bias, drift, and downhole fractionation were taken into account by
208 analysing standard materials every half hour throughout the analytical session. BLR-1 titanite
209 (Aleinikoff et al., 2007) was used as the primary standard for date calculations, and OLT-1 titanite
210 (Kennedy et al., 2010) as a secondary standard. For trace elements the NIST610 glass was used as
211 primary external standard and the stoichiometric Si content in titanite for internal standardisation. The
212 NIST612 glass, USGS BHVO 2G and BCR 2G were analysed throughout the analytical session to
213 check precision and accuracy of the results.

214 3.3.1 Zr-in-titanite thermometry

215 In order to assess (re)crystallisation temperatures in titanite, we used the Zr -in-titanite method using
216 the calibration in Hayden (2008). Analytical uncertainties on Zr measurements are from 5-10 % (2σ)
217 which gives temperature uncertainties of 5-10 $^{\circ}\text{C}$. Pressure and activity uncertainties result in even
218 larger temperature uncertainties. Our samples lack rutile and have abundant ilmenite which has an
219 estimated $a_{\text{TiO}_2} > 0.8$ (Chambers and Kohn, 2012; Kapp et al., 2009; Kohn, 2017; Schwartz et al.,
220 2008). Pressure estimates for rocks of the Agua del Sapo complex are not available. Pressure
221 estimates for the surrounding migmatitic complexes (Tolombon and Tolombon West complexes) are
222 in the range of 6-5 kbar (Büttner et al., 2005; Finch et al., 2017). We assume a value of 5.5 kbar for
223 the titanite-bearing migmatites, as suggested by the mineral paragenesis of neighbouring Al-rich
224 migmatites that include cordierite and sillimanite. In an attempt to reflect the uncertainties, we assume
225 a minimum 2σ uncertainty of 25 $^{\circ}\text{C}$ for each datum.

226 3.4 Terminology

227 We follow Sawyer (2008) and use the term *migmatite* for any partially melted rock, *metatexite* for
228 migmatites that preserve the original fabric, *stromatic metatexite* for layered migmatites, *diatexite* for
229 migmatites that lost coherence due to high fraction of melt, *neosome* for rocks that underwent partial

230 melting, *leucosome* for the light-coloured, product of partial melting, and *melanosome* for the residual
231 part of the neosome from which melt was extracted. Mineral abbreviations are after Whitney et al.
232 (2010). When referring to results from geochronology, we use “date” to refer to the calculated value
233 from measured isotopic ratios, and “age” when the date has geological significance (following
234 Horstwood et al., 2016; Schoene et al., 2013).

235 4 Results

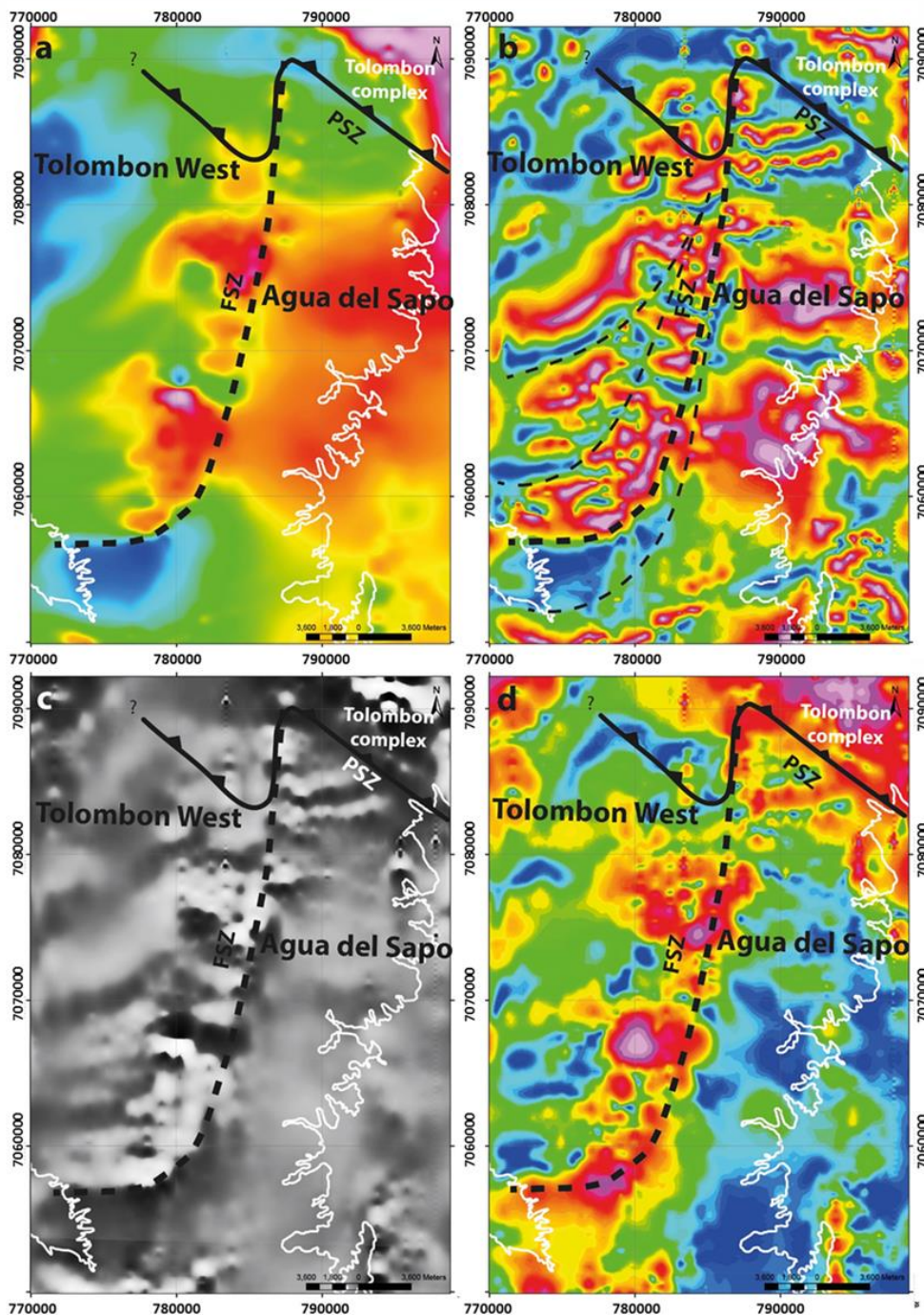
236 South Sierra de Quilmes: Tolombon West and Agua del Sapo complexes

237 The region to the south of the Pichao Shear Zone has been split here into two distinct complexes: the
238 Agua del Sapo complex proper, to the east of the mountain divide, and the Tolombon West complex
239 to the west. The two are separated by a newly mapped N-S trending shear zone up to 500m-wide, the
240 Filo Shear Zone, that crops out along the ridge of the mountain and displaces the Pichao Shear Zone
241 sinistrally with a heave of 7 km (Fig. 2). Thus, the three metamorphic complexes in the Sierra de
242 Quilmes - the Tolombon, Tolombon West and Agua del Sapo complexes - are separated by the
243 interconnected Pichao and Filo Shear Zones. This division is based on a combination of geological
244 features and supported by satellite and aeromagnetic images. We start this section by describing the
245 expression of these complexes and bounding shear zones in the aeromagnetic images. We then
246 described these two complexes, their boundaries, lithologies and structures.

247 4.1 Aeromagnetic images

248 The aeromagnetic images define two fields with different signatures (Fig. 3), corresponding to the
249 Agua del Sapo complex in the east and the Tolombon West complex in the west. The Agua del Sapo
250 complex is characterised by lower magnetic values and a smoother magnetic texture, with longer
251 wavelength variations in the RTP-TDR and RTP-1VD images, indicating the relatively low dip angles
252 of the stratigraphy. The Tolombon West complex is characterised by a mottled texture in RTP-1VD
253 and RTP-AS images, and stippled in RTP-TDR images. Compared to the Agua del Sapo complex, it
254 has overall higher magnetic intensities (RTP-AS image) and steeper gradients with shorter
255 wavelength patterns, indicating a heterogeneous distribution of magnetic rocks and steeper dip angles.

256 The difference in magnetic intensity between the two complexes is particularly clear in the south,
 257 marking the NE-SW boundary between them. The Pichao Shear Zone in the north is characterised by
 258 a low magnetic intensity corridor that contrasts with the higher magnetic values of the granulite facies
 259 rocks of the Tolombon complex further to the north.



260

261 *Figure 3. Aeromagnetic images of a section of the Sierra de Quilmes showing the contacts*
 262 *between the three complexes in Fig. 2. a) Total magnetic intensity (TMI). b) Reduced to*
 263 *pole-tilt derivative (RTP-TD). c) Reduced to pole- first vertical derivative (RTP-1VD). Note*

264 *the asymmetric magnetic gradient of rocks dipping NW in the Tolombon West complex. d)*
265 *Reduced to pole- analytical signal (RTP-AS). Note the distinct change in the magnetic signal*
266 *across the mountain range from west to east, with the Agua del Sapo complex having lower*
267 *magnetic values in contact with an irregular N-S band of high magnetic rocks following the*
268 *Filo Shear Zone in the RTP-1VD. Aeromagnetic data provided by SEGEMAR, the*
269 *Argentinian Geological Service.*

270 4.2 Tolombon West complex

271 This complex is separated from the Tolombon complex by the western section of the Pichao Shear
272 Zone, and from the Agua del Sapo complex by the Filo Shear Zone (Fig. 2). The rock types here are
273 Al-rich siliciclastic turbidite package with minor calc-silicate rocks, similar to the Tolombon
274 complex, now dominated by migmatites. There is a gradual increase in leucosome volume from west
275 to east, that eventually form irregular granite bodies. This is followed by an increase in finite strain
276 marked by more intense foliation, defined by metamorphic minerals associated with migmatization
277 and reinforced by leucosomes.

278 In the west, migmatites are melanocratic, restitic metatexites interlayered with 5-10 m wide bands of
279 nebulitic metatexites and mesocratic schollen diatexites. The restitic metatexites are folded and
280 preserve the original compositional layering of the turbiditic protolith. Where restitic metatexites
281 dominate, there are regularly-spaced lenses of leucosome subparallel to the axial surface of N-S
282 trending folds (Fig. 4a). These restitic metatexites are dominated by biotite, cordierite, sillimanite,
283 plagioclase, and K-feldspar with ~20 modal % of quartz and rare scattered garnet (Fig. 4b).

284 Towards the east, the metatexite transitions to diatexite. This is coupled with the disappearance of
285 cordierite and an increase in modal content of garnet. There are, however, round nodules of
286 Sil+Bt+Grt that could represent pseudomorphs after cordierite (Fig. 4b). In this area, as in the Agua
287 del Sapo complex, there are leucosomes of tonalitic composition crosscutting migmatitic bedding
288 (Figs. 4d and 4e). Unlike other rock sequences, here magnetite-rich diatexite migmatites dominate
289 (Fig. 2). They are associated with pegmatites with 5 cm-wide patches of magnetite, and are reflected
290 in the high magnetic susceptibility values of this area (Fig. 3). Pegmatites and irregular granitic bodies
291 are broadly parallel to the main foliation (Fig. 2). The large San Antonio granite stock in the north of
292 the complex is a leucogranite hosted by Crd-bearing schists and characterized by magmatic layering
293 defined by tourmaline, biotite and garnet.

294 The migmatites across the Tolombon West complex have a garnet-cordierite-sillimanite paragenesis,
295 similar to parts of the neighbouring Tolombon complex, suggesting temperatures between 650-750 °C
296 and pressures below 5 kbar (Büttner et al., 2005). Unlike the Tolombon complex, there is no evidence
297 of granulite-facies conditions marked by the presence of orthopyroxene. Rocks of the Tolombon West
298 complex are marked by a strong retrogression of peak metamorphic assemblages where cordierite and
299 garnet are partially replaced by biotite-sillimanite (Fig. 4b), and sillimanite and K-feldspar are
300 commonly replaced by 2-3 cm poikiloblasts of muscovite, commonly randomly oriented.

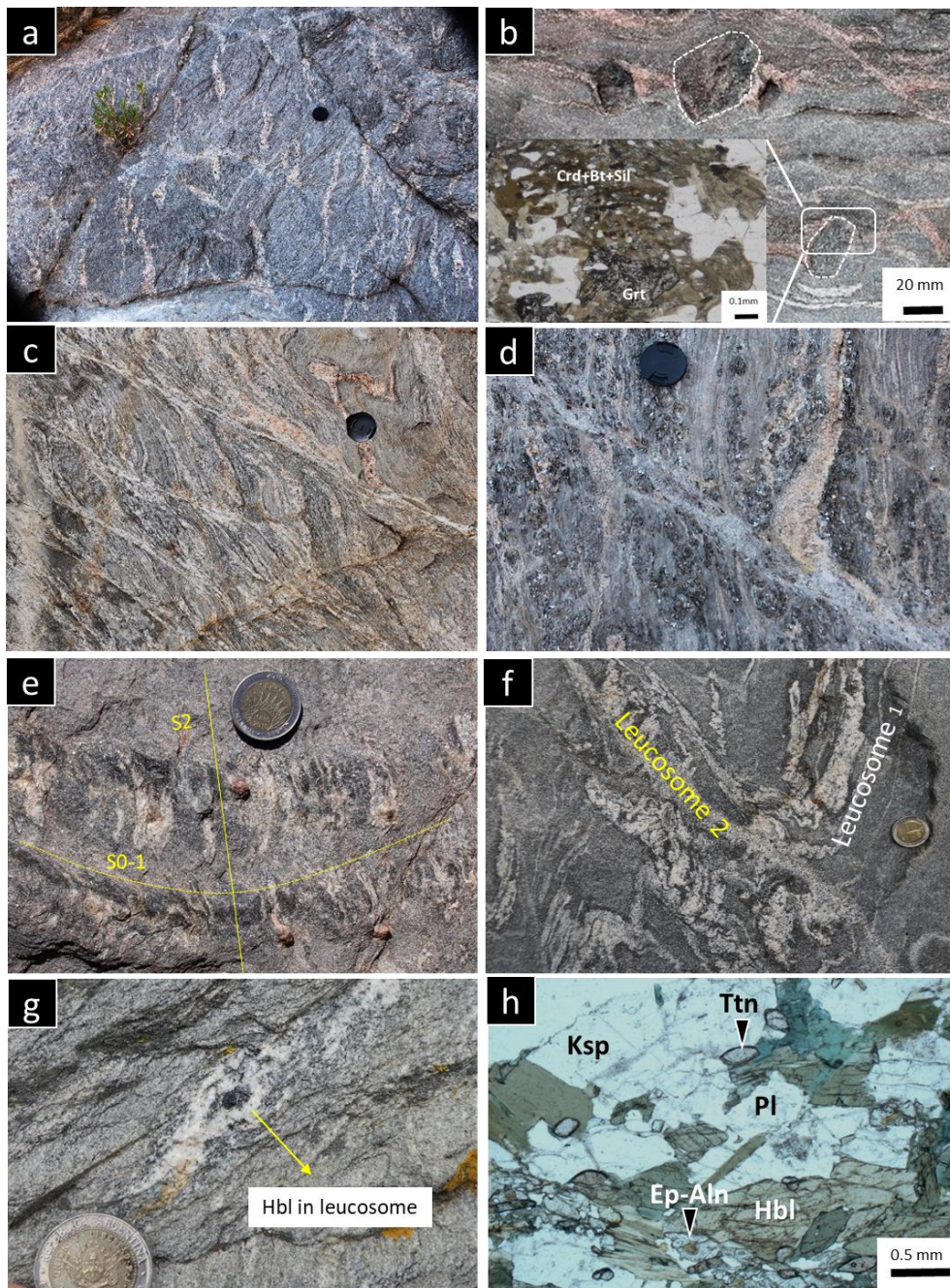
301 4.3 Agua del Sapo complex

302 The Agua del Sapo complex in the footwall of the Pichao Shear Zone and east of the vertical Filo
303 Shear Zone (Fig. 2) encompasses a suite of strongly deformed metasedimentary rocks. The bulk
304 composition and the metamorphic grade of these rocks vary from north to south. In the north, in the
305 immediate footwall of the PSZ, the rocks are garnet-biotite schists and sillimanite paragneisses of
306 amphibolite facies similar to the sub-solidus rocks of the Tolombon complex. The transition from
307 schist to paragneiss is coupled with the first appearance of sillimanite (Fig. 4e), which increases in
308 modal content towards the south. Approximately 10 km south of the PSZ, near Talapaso village (Fig.
309 2), metatexite migmatites mark the onset of partial melting evidenced by discrete 2-5 cm-wide
310 leucosome lenses at high angle to bedding (Fig. 4f). The change in metamorphic grade is marked by a
311 southward increase in magnetic values visible in Figs. 3a, b.

312 Some 20 km south of the PSZ, these rocks grade to Hbl+Ep+Aln+Ttn-bearing metasedimentary rocks
313 (Fig. 4h). We refer to these rocks as Ca-rich siliciclastic rocks. They have interlayered pelitic and
314 psammitic beds preserving graded bedding, and are interpreted to represent metamorphosed
315 turbidites. The onset of partial melting in these rocks (marked in Fig. 2) is indicated by discrete
316 leucosomes and increase in grain size to an average of 1-2 mm, with only minor changes in the bulk
317 mineralogy, as well as the appearance of clinopyroxene and rare Ca-rich scapolite (meionite). They
318 typically have variable but limited volumes of leucosome (up to 10-15% in area) (Fig. 4g).

319 Peraluminous two-mica granites, are common in the vicinity of the FSZ (Fig. 2). These granites are
320 elongated north-south, weakly foliated and concordant with the country-rock foliation. The

321 mineralogy includes garnet, biotite, sillimanite and muscovite, with accessory zircon, monazite, and
 322 rare apatite.



323

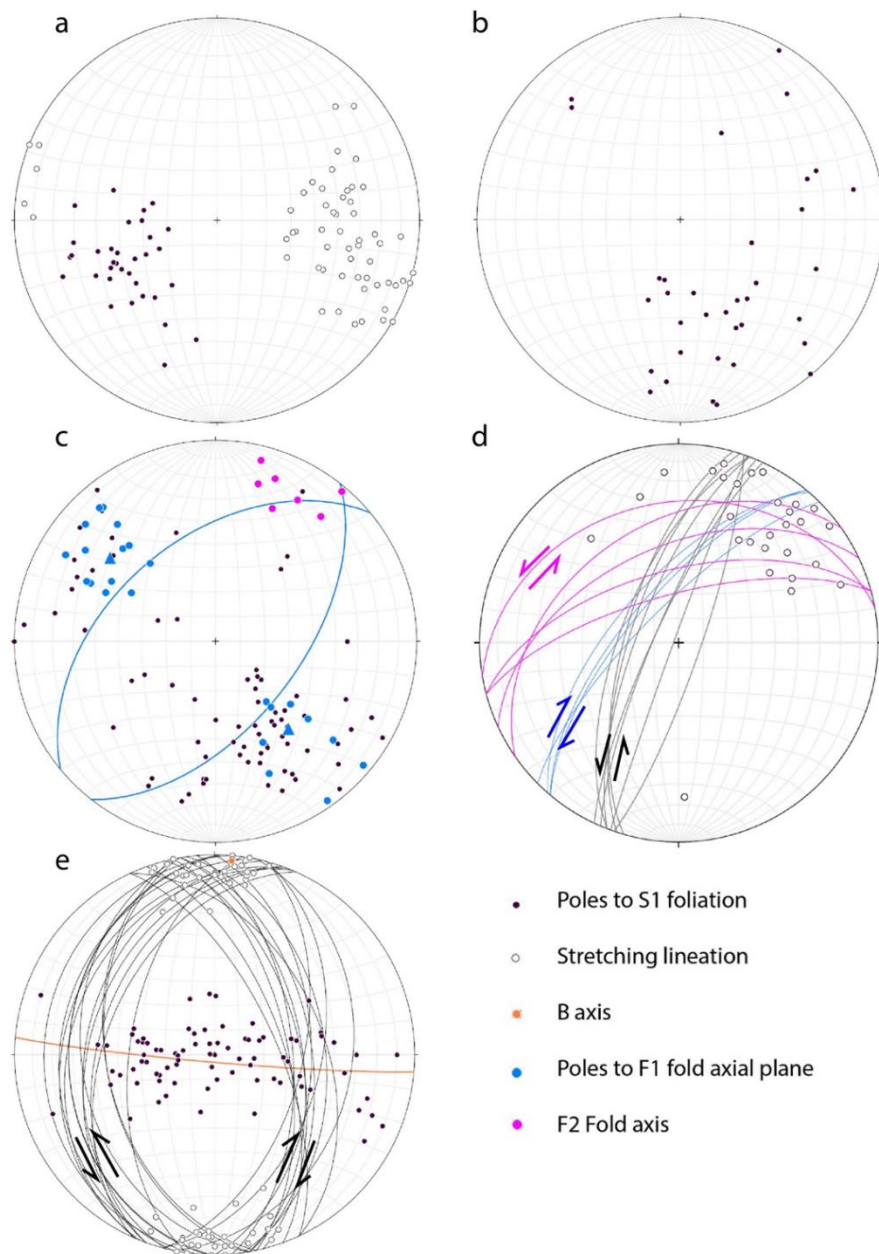
324

325 *Figure 4. (a-d) Tolombon West migmatites. (a) Restitic migmatite with a set of regularly*
 326 *spaced leucosomes 20-25 cm long, oriented sub-parallel to the axial surface of folds*
 327 *(vertical in the photograph) and at an angle to the dominant foliation. (b) Retrogressed*
 328 *cordierite porphyroblasts up to 5 cm across, now biotite-sillimanite-cordierite cored by garnet*
 329 *(inset photomicrograph). Note the thin leucosome surrounding and connecting*
 330 *porphyroblasts forming a layer. (c) Thin leucosomes in shear planes parallel to the Filo*
 331 *shear zone. (d) Two sets of leucosome overprint each other in migmatite: early, foliation-*

332 *parallel granitic leucosomes are overprinted by later, thinner tonalitic, net-veined*
333 *leucosomes. (e-f) Agua del Sapo Al-rich siliciclastic rocks. (e) Grt-Bt-Sil aggregates aligned*
334 *parallel to S₂, at a high angle to bedding. (f) Two sets of leucosome overprint each other in*
335 *migmatite: leucosome 1 is parallel to bedding with a melanosome rim, and leucosome 2*
336 *crosscuts all structures and has diffuse margins against host rocks. (g-h) Agua del Sapo Ca-*
337 *rich siliciclastic rocks. (g) Qtz+Mc+Hbl leucosome in sheared migmatite where the neosome*
338 *comprises Hbl+Pl+Ep+Aln+Ttn+Ksp. Peritectic Hbl is larger and euhedral when compared to*
339 *Hbl grains in neosome. (h) Typical mineral paragenesis and texture of Ca-rich migmatite.*

340 4.4 Structures

341 The ductile structures of the Tolombon West and Agua del Sapo complexes provide a complementary
342 record to that of the Tolombon complex where west-verging thrusts and folds were coeval with
343 anatexis (Finch et al., 2017). The structural record of the Tolombon West is markedly different from
344 that of the Agua del Sapo, being dominated by folds with local shear zones, whereas the Agua del
345 Sapo complex is dominated by a very distinctive prolate deformation with an intense stretching
346 lineation and intense simple shear deformation.



347

348 *Figure 5. Stereonet projections of foliation and lineation from the Sierra de Quilmes. Data*
 349 *from: (a) Tolombon complex showing a well-defined lineation associated with W-verging*
 350 *thrusts (data from {Finch, 2015 #259}). (b) North section of the Tolombon West. The west-*
 351 *dipping foliation is from areas near the Filo shear zone and the north-dipping foliation from*
 352 *the west side of the complex. (c) South part of the Tolombon West complex. Poles to fold*
 353 *axial planes with leucosomes (blue dots) are parallel to S1 (black poles), and cluster in two*
 354 *groups indicating two limbs of F2 folds. Blue great circles are the mean plane from each pole*
 355 *cluster which intersect in the NE, close to shallow plunging F2 fold axes. (d) Shear zones in*
 356 *Tolombon West complex. Blue great circles indicate dextral shear zones, purple indicates*
 357 *sinistral shear zones and black indicates the sinistral splays from the Filo shear zone. (e)*
 358 *Agua del Sapo complex. Black great circles represent shear zones: dextral when dipping to*
 359 *the east and sinistral when dipping to the west. Together they define limbs of F2 folds and*
 360 *their B axis is parallel to the stretching lineation.*

361 4.4.1 Structures in the Tolombon West complex

362 The Tolombon West complex, bound by the two shear zones (Fig. 2), can be divided into a northern
363 and the southern section based on structural style. The limit between the two is diffuse and around the
364 town of Toro Yaco (Fig. 2). The structures in the northern section are similar to those of the
365 Tolombon complex (Fig. 5a), dominated by syn-anatectic fold and thrusting to the west. The
366 dominant foliation, S1, is parallel to bedding (Fig. 5b), associated with F1 isoclinal folds and top-to-
367 west shear zones. Foliation strikes N-S and dips west near the FSZ, and rotate to a NE-SW trend,
368 dipping NW, away from the shear zone. F1 folds are associated with leucosomes parallel to the axial
369 planes (Fig. 6a), suggesting that the folds were syn-anatectic. Unlike the Tolombon complex, there are
370 sinistral shear zones dipping moderately to the NW with a mineral lineation, mostly sillimanite, that
371 plunges between 10-30° NE. These are relatively narrow (2-5 m wide) mylonitic to proto-mylonitic
372 shear zones, and a few of them have 20-30 cm thick ultramylonitic bands. The presence of sillimanite
373 on the shear planes indicates high-grade metamorphic conditions, as with the thrusts in the Tolombon
374 complex (Büttner et al., 2005; Finch et al., 2015). In the west, where S1 dips NW, there are metric-
375 scale N-S trending, upright, open folds with leucosomes in their axial planes, parallel to a new S2
376 foliation, related to a second folding event (F2).

377 In the southern section, the fabric rotates from N-S to NE-SW following the curved trace of the Filo
378 Shear Zone (Fig. 2). The F1 isoclinal folds rotate with the foliation, and like the northern section, they
379 typically have axial planar leucosome veins and cusped fold hinges (Fig. 6a), and are sub-parallel to
380 S1. However, unlike the northern section, F1 and S1, are overprinted by km-scale upright F2 folds
381 plunging 5-10° to the NE, and an inter-limb angle of ~75° (Fig. 5c). The axial planar foliation, S2, is
382 defined by elongated porphyroblasts of the high-temperature minerals cordierite, fibrolite sillimanite,
383 and biotite. In some places, S2 is coupled with leucosomes showing continued anatexis (Fig. 6b).

384 In the south, there are also shear zones parallel to S1, however their kinematic is variable. Some 5 km
385 to the south of Toro Yaco town (Fig. 2) there are 1-2 m-thick sillimanite-bearing dextral shear zones
386 that dip ~70° NW and overprint F2, deflecting their trace by a few centimetres. To the east and south
387 of these dextral shear zones, there are sub-vertical sinistral shear zones that are part of the splays of

388 the Filo Shear Zone. Both sets of shear zones are parallel to the F2 axial planes and their mineral
389 stretching lineation, mostly defined by sillimanite and stretched mineral aggregates, plunge $\sim 30^\circ$ NE
390 (Figs. 2 and 5d).

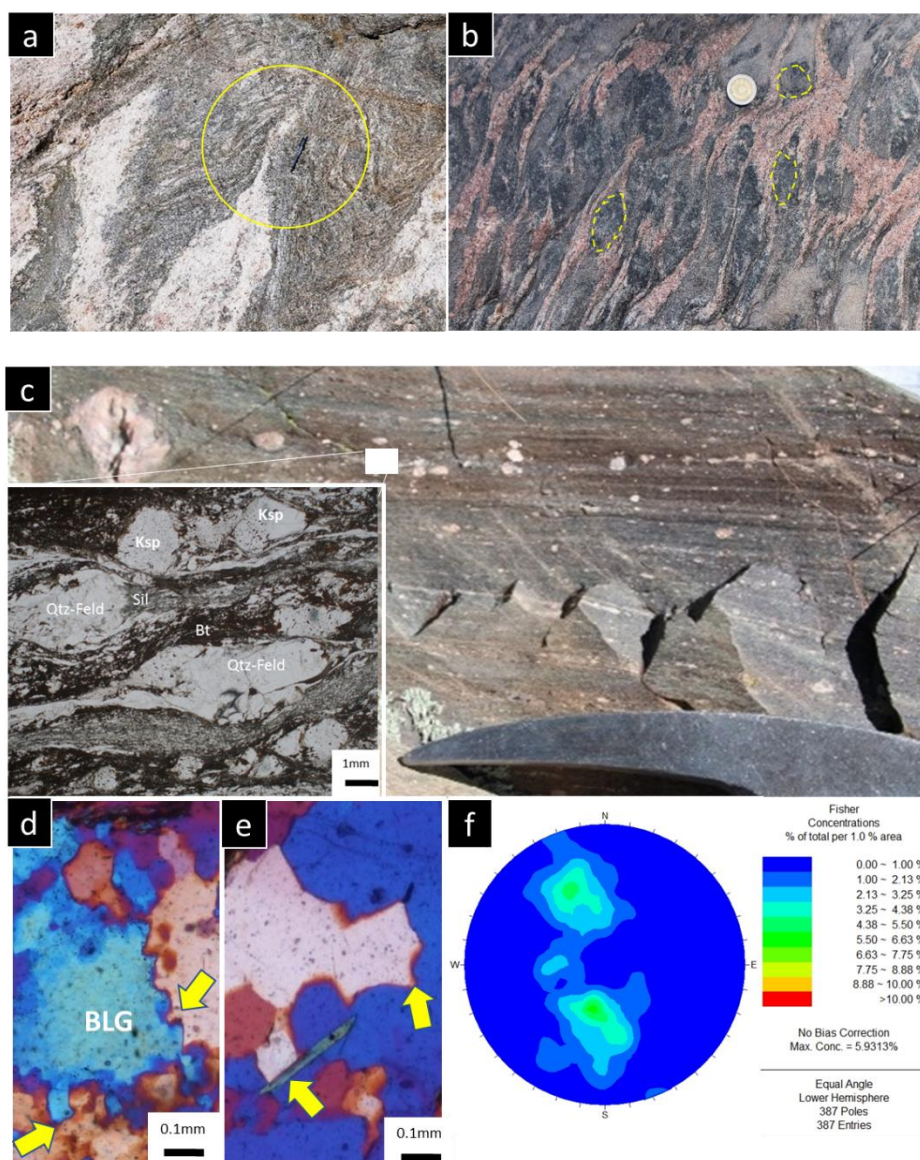
391 4.4.2 *Filo Shear Zone*

392 The trace of the sub-vertical Filo Shear Zone in the aeromagnetic images (Fig. 3) defines a broad,
393 curved shape, similar to the S1 foliation described above, rotating gradually from a north-south to an
394 east-west orientation, where it ends as numerous splays in the south marked by the 2-5 m-thick
395 mylonitic bands described above (Fig. 2). In the northern section, its width is ~ 500 m and records
396 intense deformation producing a ~ 200 m thick black, ultramylonitic rock with naked clasts, similar to
397 those in the Pichao Shear Zone (Fig. 6c). Further to the north it displaces and merges with the Pichao
398 Shear Zone (PSZ) deflecting it by ~ 7 km sinistrally. Its sinistral kinematics is indicated by σ -shaped
399 prophyroclasts of feldspar and garnet, muscovite fish, and shear bands formed by biotite-sillimanite
400 (Fig. 6c). Along most of its length, the mylonitic rocks have lower amphibolite facies paragenesis,
401 and deforms both the Al-rich and the Ca-rich siliciclastic rocks of the Agua del Sapo complex,
402 including rocks with stretched hornblende, epidote and allanite. Where it merges with the Pichao
403 Shear Zone, there is a greenschist facies overprint with chlorite in the matrix (see also Finch et al.,
404 2015). In this region, the core of the shear zone has a gently NNE-plunging lineation in a subvertical
405 sinistral shear zone. Outwards from this core zone, the lineation rotates towards W- or E-plunging,
406 and the ultramylonitic foliation becomes moderately dipping recording top-to-W motion, suggesting
407 that the earlier, top-to-West Pichao Shear Zone was rotated and overprinted by the sinistral motion of
408 the Filo Shear Zone.

409 The ultramylonite of the FSZ is typically characterised by a matrix that is reasonably homogeneous
410 with only short quartz ribbons (Kilian et al., 2011) while the Kfs porphyroclasts are mantled by
411 recrystallized K-feldspar and myrmekites. Quartz shows dominant recrystallisation by grain boundary
412 migration (GBM) and strong crystallographic preferred orientation (CPO) (Fig. 6e and f). Quartz also
413 shows evidence for bulging (BLG) (Fig. 6d).

414 4.4.3 Structures in the Agua del Sapo complex

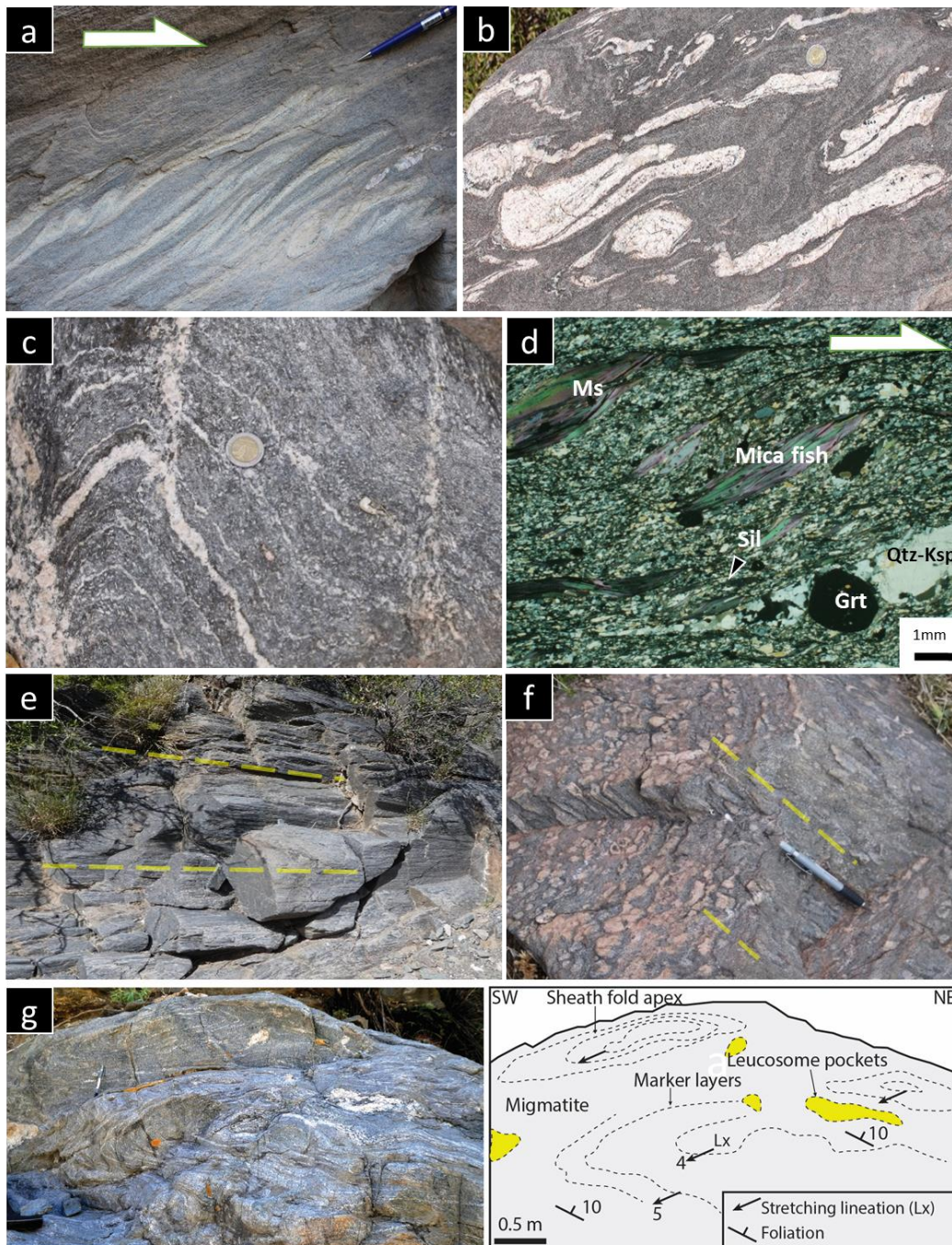
415 Deformation in the Agua del Sapo complex is different from the other complexes. The Agua del Sapo
 416 complex is dominated by intense shearing with top-to-south transport (Fig. 7a,b and d) and an intense
 417 N-S trending lineation (Fig. 7e,f). These structures overprint earlier ones preserved in lithons, that are
 418 typical of the hanging wall Tolombon complex (D1), and therefore mark a D2 event. This is the last
 419 major event and is followed by a much weaker D3 event represented by a set of 1-5 m wide, sub-
 420 vertical greenschist facies dextral shear zones striking north-south, in the eastern edge of the complex
 421 (Fig. 2). Here, we describe the two major deformational events in this complex.



422

423 Figure 6. (a-b) Structures in the Tolombon West complex. (a) F1 cusped hinge in isoclinal
 424 folds with leucosome on the axial surfaces. (b) Leucosome controlled by S2, wrapping

425 around large cordierite porphyroblasts, marked by yellow dashed ellipses. (c-f) Filo Shear Zone.
 426 Zone. (c) Ultramylonite hand-sample with photomicrograph in plane-polarized light (inset).
 427 Quartz-feldspar aggregate form clasts with recrystallized tails parallel to bands of biotite-
 428 sillimanite. (d-f) Photomicrographs with cross-polarized light and gypsum plate representing
 429 samples of shear zones. (d) Lobate margins of recrystallised quartz, suggesting the onset of
 430 bulging (BLG). (e) Grain boundary migration (GBM) of quartz evidenced by cusped and
 431 lobate borders and pinning by mica grain (yellow arrows). (f) Stereogram of quartz c-axis
 432 orientation from the FSZ mylonite showing strong preferred orientation defining two maxima
 433 that define a weak girdle.



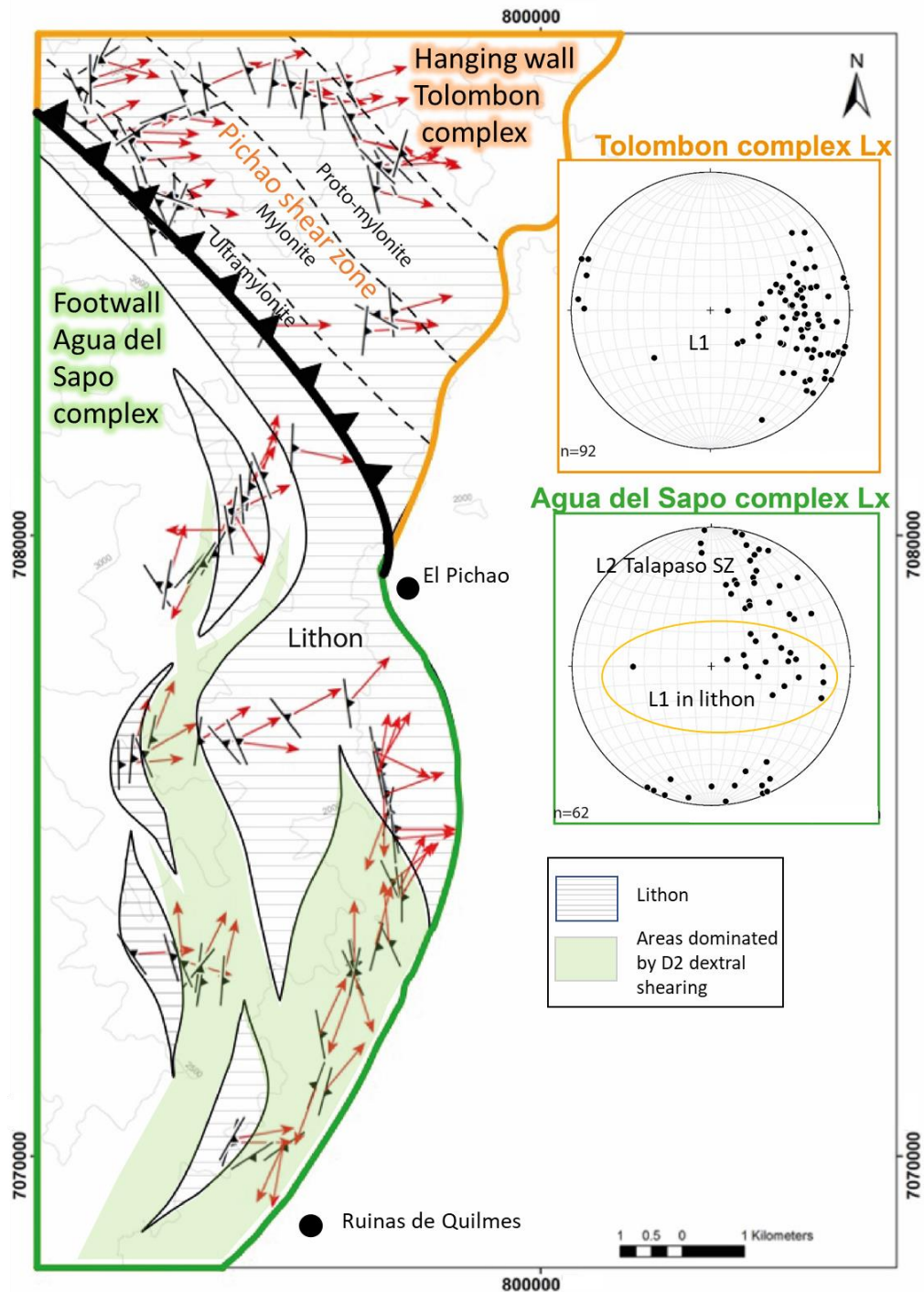
434

435 *Figure 7. Structures of the Agua del Sapo complex. (a) Tight fold train with vergence to the*
 436 *right (top-to-south) in amphibolite facies metasedimentary rock. (b) Same for strained and*
 437 *partly disaggregated pegmatites in psammite. (c) Upright F2 fold with leucosome in axial*

438 *planar foliation. (d) Photomicrograph of a schist showing dextral motion (top-to-south)*
439 *indicated by mica fish and asymmetric tails around garnet. (a, b and d) are parallel to*
440 *lineation and perpendicular to foliation and consistently indicate top-to-south. (e-f) L-*
441 *tectonites in different rock-types: e) Metapsammite. f) Metapelite with stretched quartz and*
442 *feldspars showing the absence of a foliation. (g) Sheath folds parallel to stretching lineation*
443 *and diagram to the right showing details. Leucosomes are either folded with the dominant*
444 *foliation or form pockets elongated parallel to fold axis and Lx.*

445 D1 structures

446 The earliest structure in this complex is a metamorphic foliation parallel to bedding (S1), that is only
447 preserved in lithons. These lithons occur in the north (Fig. 8) and their size and frequency decrease to
448 the south, where D2 becomes more intense. S1 is defined by muscovite, biotite and sillimanite in the
449 Al-rich siliciclastic rocks, and biotite and hornblende plus elongated epidote-allanite grains in the Ca-
450 rich ones. Leucosomes are axial planar, and cross cut the hinge of isoclinal folds (F1) suggesting that
451 folding was contemporaneous to peak metamorphism and anatexis. Stretching lineation plunges east
452 and is associated with top-to-west kinematics. Thus, D1 structures are similar in orientation, high-
453 grade paragenesis and kinematics to structures in the Tolombon complex. The transition between
454 lithons and rocks dominated by D2 structures is sharp, and defined by the progressive rotation of the
455 stretching lineation over 1 to 2 metres across strike.



456

457 Figure 8. Lithons in the footwall Agua del Sapo complex below the Pichao Shear Zone.
 458 Green fields are regions dominated by strongly deformed rocks (D2) marked by dextral
 459 shearing along sub horizontal lineations defining the Talapaso SZ (Fig. 2) and horizontal
 460 stripes mark less deformed lithons preserving the older top-to-west sense of shear dominant
 461 in the Tolombon Complex and the Pichao Shear Zone with E-plunging lineations.
 462 Stereographic projections show stretching lineation measured in the Tolombon and Agua del
 463 Sapo complex.

464 D2 structures

465 Shear zones and stretching lineation (L2)

466 The Agua del Sapo complex is generally strongly sheared with a well-defined lineation sub-horizontal
467 N-S that can be seen from a distance (Fig. 2). Given the rock types, particularly the psammites, it is
468 not always possible to ascertain strain intensity. However, markers like pegmatites and leucosome
469 veins are strongly stretched or folded (Fig. 7a-b) and tend to be mylonitic, indicative of high-strain
470 zones. We have tentatively defined two main high-strain corridors parallel to the Filo Shear Zone: the
471 Talapaso Shear Zone to the east and the Catalino Shear Zone to the west (Fig. 2 and 8). They both
472 have the same dominant horizontal, N or S plunging stretching lineation. The Talapaso Shear Zone
473 dips $\sim 45^\circ$ E and has a dextral shear sense, whereas the Catalino Shear Zone dips $\sim 35-40^\circ$ W and has a
474 sinistral shear sense. Thus, they both record top-to-the-south kinematics. Like the Filo Shear Zone, the
475 Catalino Shear Zone seems to merge with the Pichao Shear Zone. The Talapaso and Catalino Shear
476 Zones are typically 500 m wide mylonitic zones that transition into proto-mylonites across strike. The
477 strain profile in these shear zones is asymmetric with a sharp strain gradient in the footwall and a
478 wider gradient towards the hanging wall. In between these major shear zones, there are several
479 parallel proto-mylonitic corridors with consistent top-to-south movement, independent of their dip
480 direction. The most typical kinematic indicators are asymmetric shear folds (Fig. 7a-b), σ -shaped
481 porphyroclasts of feldspars, muscovite fish (Fig. 7d), asymmetric strain shadows around garnet and
482 other mineral aggregates, and C' shear bands formed by biotite-sillimanite. The mineral lineation (L2)
483 plunges 0 to 10° to the north or south (Fig. 5e), and is defined by elongated quartz-feldspathic
484 aggregates, micas, and tourmaline.

485 The strongly strained pegmatites and leucosomes in the shear zones have both quartz and feldspars
486 ductily stretched. Quartz is recrystallised by sub-grain rotation (SGR), characterised by a strong
487 oblique fabric defined by new grains or well-defined undulose extinction (Passchier and Trouw,
488 2005). There are also quartz ribbons along the main mylonitic foliation and areas where quartz
489 crystals have straight grain boundaries and lack undulose extinction indicative of static
490 recrystallisation, or grain boundary area reduction (GBAR similar to that in Fig. 6e). Feldspar

491 porphyroclasts are mantled by fine recrystallised grains and have myrmekites where it faces the
492 shortening direction.

493 Upright folds (F2)

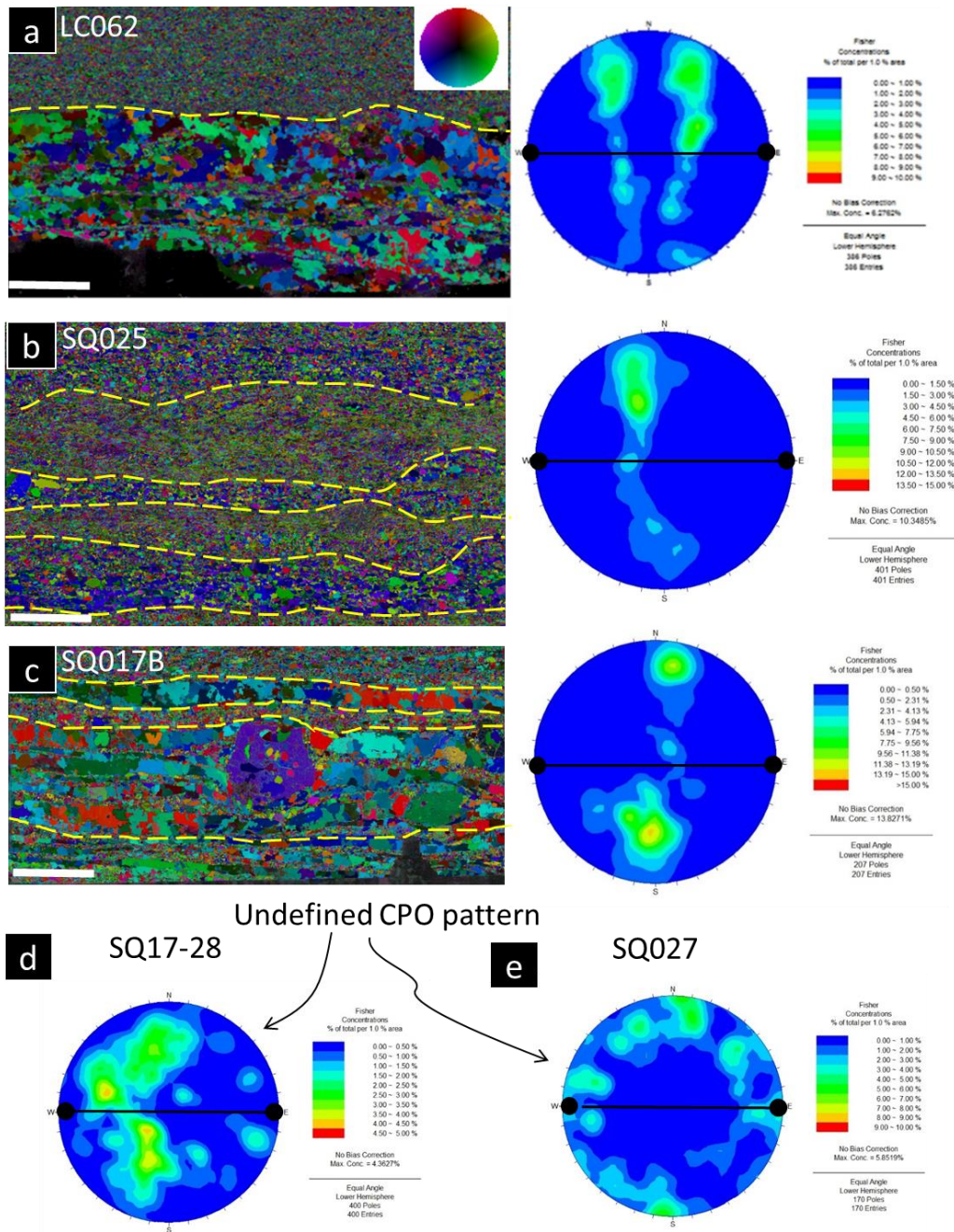
494 The opposite dip directions of the two major shear zones described above, as well as changes in the
495 broader foliation distribution define km-scale N-S trending upright folds (F2) (Fig. 5e). These are also
496 present at smaller scale (Fig. 7c), similar to the ones in the southern Tolombon West complex. In the
497 east of the Agua del Sapo complex, they are open folds, with a 2-5 km wavelength, grading to close
498 folds with a 0.5-0.1 km wavelength in the west, near the Filo Shear Zone. The intensity of S2 axial
499 planar foliation also increases westwards, coupled with the tightening of fold inter-limb angle (lower
500 cross section in Fig. 2). The F2 fold axis is parallel to the stretching lineations (L2) in the shear zones
501 and plunges gently north or south, defining large-scale doubly-plunging folds or elongated domes
502 (Fig. 2). The core of these domes expose the highest grade rocks in the complex, and coincide with
503 the two large magnetic anomalies in the RTP_TD (Fig. 4). The axial planar foliation (S2) cross-cuts
504 S0/S1 (Fig. 4e) and can be observed at scales from satellite to microscopic. S2 is defined by biotite
505 and sillimanite, and L2 by elongated mineral aggregates (Bt-Sil rimming Grt) parallel to the fold axes.
506 In relatively rare outcrops, the F2 axial plane has leucosome veins (Fig. 7c) suggesting that incipient
507 anatexis occurred during D2.

508 L and L>S tectonites and sheath folds

509 In between the Talapaso and Catalino Shear Zones, there are kilometric domains characterized by L-
510 and L>S tectonites (Fig. 7e-f) dominated by a N-S, low pitch stretching lineation. In these rocks, long
511 minerals such as amphibole, tourmaline and sillimanite, define a lineation whereas the basal cleavage
512 of micas lack preferred orientation. They are commonly associated with sheath folds (Fig. 7g),
513 variable in size (0.5 to 3 m) and shape, and stretched parallel to L-tectonites, many with acute hinge
514 angles, lower than 20°. This tight sheath folds are classified as tubular folds (Skjernaa, 1989) and here
515 they have their fold hinge pointing to the south.

516 Quartz crystallographic preferred orientation (CPO)

517 In order to determine whether the linear fabric is a result of constriction or another mechanism, such
518 as overprinting deformation phases (Ramsay and Huber, 1983), we analyzed the crystallographic
519 preferred orientation (CPO) of quartz-rich bands (> 90% quartz) of L-tectonites (Heilbronner and
520 Tullis, 2006; Pennacchioni et al., 2010). The CPO pattern for quartz-rich layers shows cleft-girdles or
521 a vertical single-girdle (Fig. 9a and b, respectively). The difference between those two patterns
522 reflects the variable c-axis opening angle, which increases as a function of deformation temperature,
523 as rhomb $\langle a \rangle$ and basal $\langle a \rangle$ slip become more important (Sullivan and Beane, 2010). Figure 9a
524 shows a quartz c-axis CPO pattern that correspond to constriction, and Figs. 9b and c show similar
525 contrictional pattern with a slightly oblique single-girdle, typical of simple shear (Lister and Hobbs,
526 1980; Sullivan, 2009, 2013). The oblique single-girdle suggests that quartz was affected by a
527 component of non-coaxial deformation (Lister and Hobbs, 1980; Passchier and Trouw, 2005; Sullivan
528 and Beane, 2010). In samples with >10 % mica, the CPO pattern becomes diffuse most likely because
529 of the influence of other phases in pinning quartz and modifying local conditions (Hunter et al.,
530 2016)(Fig. 9d and 9e).



531

532 *Figure 9. CPO pattern for samples of quartz-rich L-tectonites. Data collected in thin sections*
 533 *cut parallel to lineation and perpendicular to the foliation. (a-c) C-axis orientation image of*
 534 *thin sections to the left and stereograms of the c-axis to the right. The colour of every grain*
 535 *represents its c-axis orientation in space (top right corner colour-coded circle). The sections*
 536 *analysed in every sample are the coarser-grained quartz-rich layers marked by yellow*
 537 *dashed lines. These layers contained < 10 % of other mineral phases and are several quartz*
 538 *grains in width. The reference frame in the stereograms is defined by the E-W vertical*
 539 *foliation plane (black line) and the horizontal lineation represented as black dots. (a) This*
 540 *sample shows two parallel single-girdles or "cleft girdle" typical of constrictional strain. (b, c)*
 541 *Slightly oblique single-girdle, typical of simple shear. (d-e) Stereograms from samples with >*
 542 *10% mica and feldspar showing ill-defined CPO (d), or no CPO pattern at all (e).*

543 4.5 Titanite geochronology

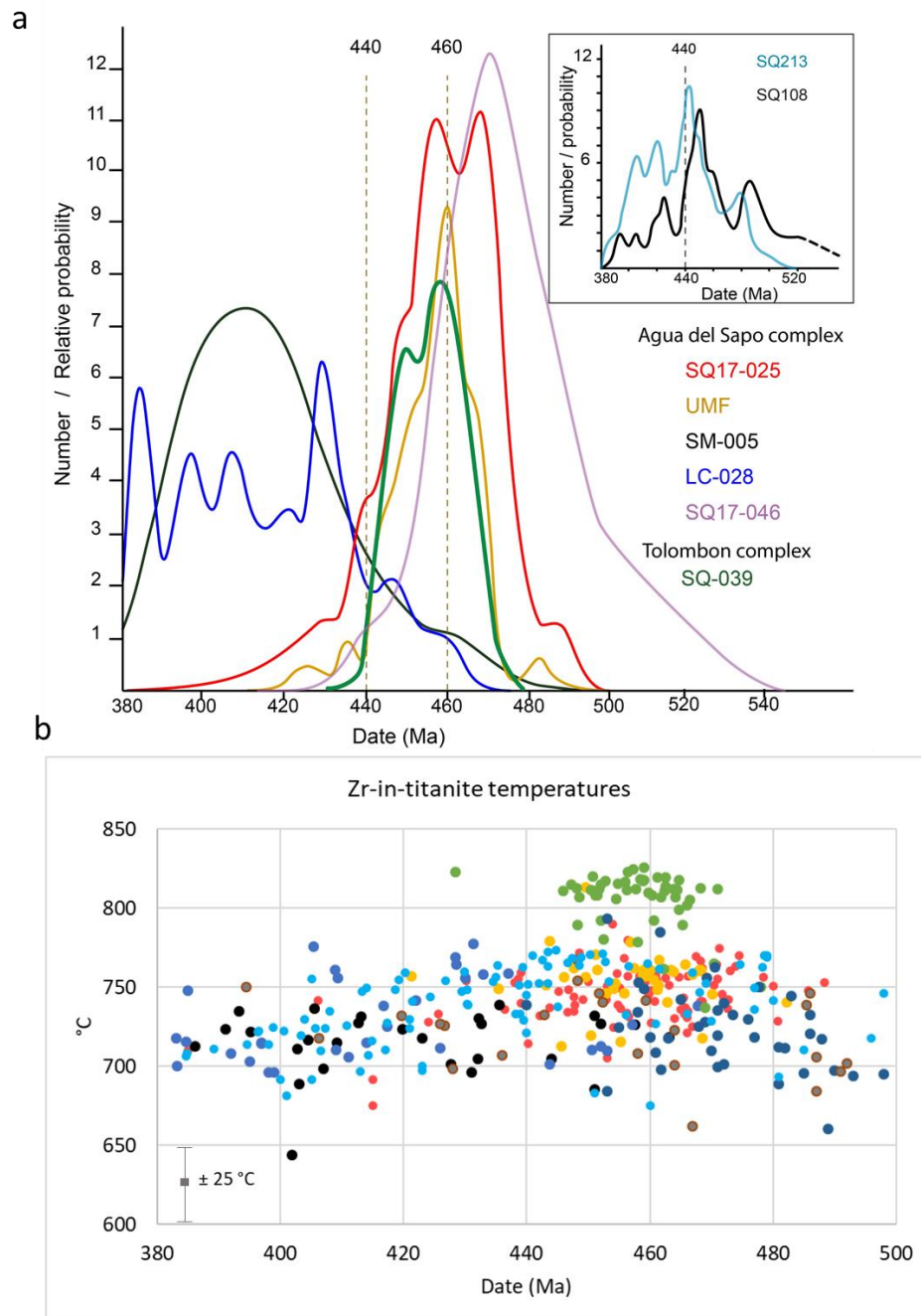
544 LASS-ICP-MS spot analysis was conducted for titanites from seven different Ca-rich siliciclastic
545 rocks, some in-situ and some from mounted separates (Supporting information). An eight sample, of
546 calc-silicate sample from the granulite facies rocks in the Tolombon complex (sample SQ-039) was
547 analysed for comparison (Büttner et al., 2005). Most of the titanite grains are 100-150 μm in size,
548 euhedral to subhedral with aspect ratios between 1 and 4. The corrected $^{207}\text{Pb}/^{206}\text{Pb}$ date of every spot
549 was defined as the lower intercept of the anchored Discordia line with the Concordia in a Tera-
550 Wasserburg diagram. The Discordia is also anchored to a $^{207}\text{Pb}/^{206}\text{Pb}$ value of 0.86 based on the model
551 evolution of Stacey and Kramers (1975) for ~470-440 Ma. To visualize the dates distribution the
552 corrected $^{207}\text{Pb}/^{206}\text{Pb}$ dates were plotted in a probability plot (Fig. 10a).

553 The seven titanite-bearing samples analysed from the Agua del Sapo complex are similar amongst
554 them. They share the same grain-size between 0.2-0.5 mm, and mineralogy
555 (Qtz+Hbl+Bt+Kfs+Pl+Ms+Ep with Cal+Ap+Ttn+Aln+Ilm as accessory phases), which is suggestive
556 of similar peak metamorphic conditions. They all show similar structures, marked by a well-defined
557 foliation defined by aligned hornblende, epidote and micas. All, except SQ-108, were collected in
558 areas with evidence of anatexis (Fig. 2). Finally, they all show minor retrogression, marked by minor
559 chloritization.

560 Despite the general similarities between the Agua del Sapo samples, the results define three groups,
561 with different titanite U-Pb date populations (Fig. 10a). Samples SQ17-025, UMF, and SQ17-046C
562 define a unimodal age distribution spread between 500 and 440 Ma, with few spots younger than 440
563 Ma. In contrast, samples SM-005 and SQ17-028 yield a broad peak of younger ages, ranging between
564 440 and 380 Ma, with fewer spots older than 440 Ma. The remaining two samples, SQ-213 and SQ-
565 108, cover most of the range defined by these two groups (inset in Fig. 10a). Titanite from sample
566 SQ-039, from the Tolombon complex, yields dates in the range 480-440 Ma, reinforcing the dates in
567 Büttner (2005) (Fig. 10a).

568 *Zr-in-titanite temperature*

569 The results for Zr-in-titanite thermometry in Fig. 10b show that estimated temperatures are generally
570 above 700 °C for the entire range of dates recorded by titanite. Temperature increases with time from
571 700 °C at ~500 Ma reaching a broad maximum in excess of 750 °C at ~460 Ma, and then decreases
572 steadily to ~700 °C ending at 380 Ma (Fig. 10b). Sample SQ-039 from the Tolombon complex
573 differs from the rest, with higher values and a weighted average temperature of 809.4 ± 3.7 °C, in
574 accordance with the estimated peak metamorphic conditions for the complex (Büttner et al., 2005).
575 Zr-in-titanite data are provided in the supporting information.



576

577 Figure 10. (a) Titanite U-Pb dates summarized in a probability plot. Sample SQ-039 from
 578 Tolombon complex yield dates between 480-440 Ma. For the Agua del Sapo complex,
 579 titanites from SQ17-025, UMF, and SQ17-046 yield dates in the 540-440 Ma range, while
 580 LC-028 and SM-005 have most dates in the 440-380 Ma range. Samples SQ108 and
 581 SQ213, in inset, have a much larger spread of dates (> 120 Ma), overlapping with all other
 582 samples in the complex. (b) Zr-in-titanite temperatures from the same analytical spots in (a).
 583 Sample SQ-039 from the Tolombon complex defines a high-T cluster, in line with the 800-
 584 850 °C estimated for peak metamorphism in rocks with Opx. Titanites from the Agua del
 585 Sapo complex, in contrast, show a broad gentle curve with temperatures consistently above
 586 700 °C over 120 Ma, and reaching 750 °C around 460 Ma. The pattern suggests a gentle
 587 prograde heating followed by a slow cooling.

588 5 Discussion

589 5.1 The nature of D2

590 *Deformation of the Agua del Sapo complex*

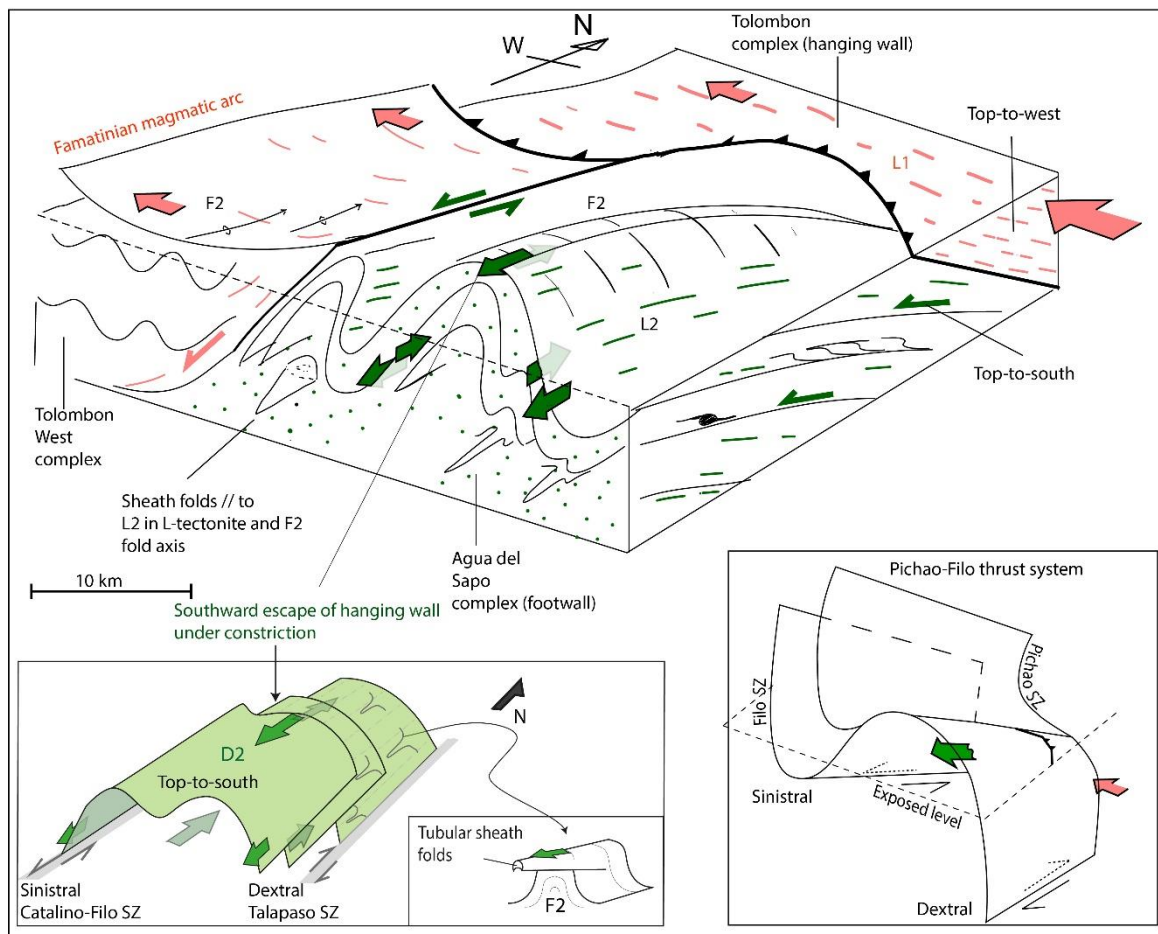
591 D1 structures preserved in lithons in the Agua del Sapo complex have been strongly overprinted by a
592 second set of structures that were not recorded in hanging wall Tolombon complex. The dominant
593 deformation features in the Agua del Sapo complex are: a) intense simple shear deformation with top-
594 to-south kinematics, b) a strong N-S subhorizontal stretching lineation associated with constrictional
595 L-tectonites, parallel to the transport direction of shear zones and the axis of sheath folds, and c)
596 upright N or S-gently plunging folds.

597 The top-to-south shear sense, independently of the dip of the foliation (e.g., Catalino versus Talapaso
598 Shear Zone in Fig. 11, lower inset), is consistent with upright folding of south-verging thrust shear
599 zones. Thus, the sinistral Filo Shear Zone, marking the westernmost boundary of this sheared terrane,
600 can be interpreted as part of a south-directed thrust that was over-steepened in the limb of a fold,
601 consistent with the observed increase in strain in its vicinity, and marked by the tightening of folds
602 (Fig. 2 lower cross-section). The exact temporal relationship between upright folding and south-
603 directed thrusting is unclear. The two could have developed together, or folding overprinted thrusting.
604 In either case, the two features can be interpreted as part of the same deformation event that achieved
605 vertical and horizontal shortening defining constriction with a N-S stretching (e.g., Fig. 3 in Bons et
606 al., 2016).

607

608 The tubular sheath folds indicate constrictional strain within shear zones (Ramsay and Huber, 1983;
609 Sullivan, 2013). Constriction is also suggested by the orientation of long minerals in combination with
610 quartz CPO patterns (Fig. 9)(Sullivan, 2013). This conclusion supports the interpretation that upright
611 folding, S-verging thrusting, N-S stretching and sheath folds, all developed broadly
612 contemporaneously as a result of a non-coaxial constrictional D2 event (Fletcher and Bartley, 1994),
613 with a N-S stretching axis and top-to-south kinematics. This phase stretched the crust parallel to the

614 orogen while translating the Tolombon complex on the hanging wall of the Pichao Shear Zone to the
 615 south.



616

617 *Figure 11. Kinematics of D1 (red arrows) and D2 (green arrows) in the Sierra de Quilmes*
 618 *with details of the Agua del Sapo complex structures. In the Tolombon and Tolombon West*
 619 *complexes west-verging thrusts related to D1 are preserved while in the Agua del Sapo*
 620 *complex D2 dominates. Here, open upright F2 folds with dextral and sinistral shear zones on*
 621 *opposite limbs define a southward tectonic transport (inset in lower left). F2 fold axis is*
 622 *parallel to stretching lineations and L-tectonites indicating a non-coaxial constrictional*
 623 *regime. Inset in lower right corner depicts the geometry of the Pichao-Filo thrust system*
 624 *folded and plunging to the north.*

625 *D2 in Tolombon West complex*

626 Unlike the Agua del Sapo complex, D2 in the Tolombon West complex lacks the intense lineation,
 627 evidence for constriction, and intense simple shear. D2 is instead expressed mostly as folding with
 628 only subordinate shearing, focused on the vicinity of the sinistral Filo Shear Zone. This shear zone
 629 defines a broad arc, rotating gradually southwards from N-S striking into smaller splays striking NE-
 630 SW, marking the contact with the lower magnetic susceptibility rocks of the Agua del Sapo complex

631 (Fig. 3). The regional foliation rotates into parallelism with the main trend of the Filo Shear Zone.
632 Also, the syn-anatectic upright F2 folds, varying from metric-scale to 100s of metres, trend parallel to
633 the Filo Shear Zone trace as it rotates. Folds become more intense to the south where they are
634 overprinted by the narrow (5-15 cm wide) sillimanite-bearing dextral shear zones parallel to S2.
635 We interpret the splaying of the Filo Shear Zone as reflecting the end of the strike-slip shear zone
636 accompanied by movement transfer into the upright folds, that intensify southwards. This movement
637 transfer caused shortening and possibly thrusting of the Tolombon West against the Agua del Sapo
638 complex to the south (Fig. 3). The NE-striking dextral shear zones, parallel to the axial planes in this
639 region of movement transfer developed in the stability field of sillimanite and their kinematics suggest
640 a NNW-SSE-driven transpression partitioned between folds and shear zone, possibly as part of the
641 same D2 event.

642 We conclude therefore that during D2 the strain ellipsoid must have changed from a prolate N-S
643 ellipsoid in the Agua del Sapo complex, with a strong simple shear component, to an oblate ellipsoid
644 with a maximum shortening oriented E-W in the north of the Tolombon West complex to NNW-SSE
645 in its south, where the influence of the movement transfer from the strike slip shear zone is
646 significant.

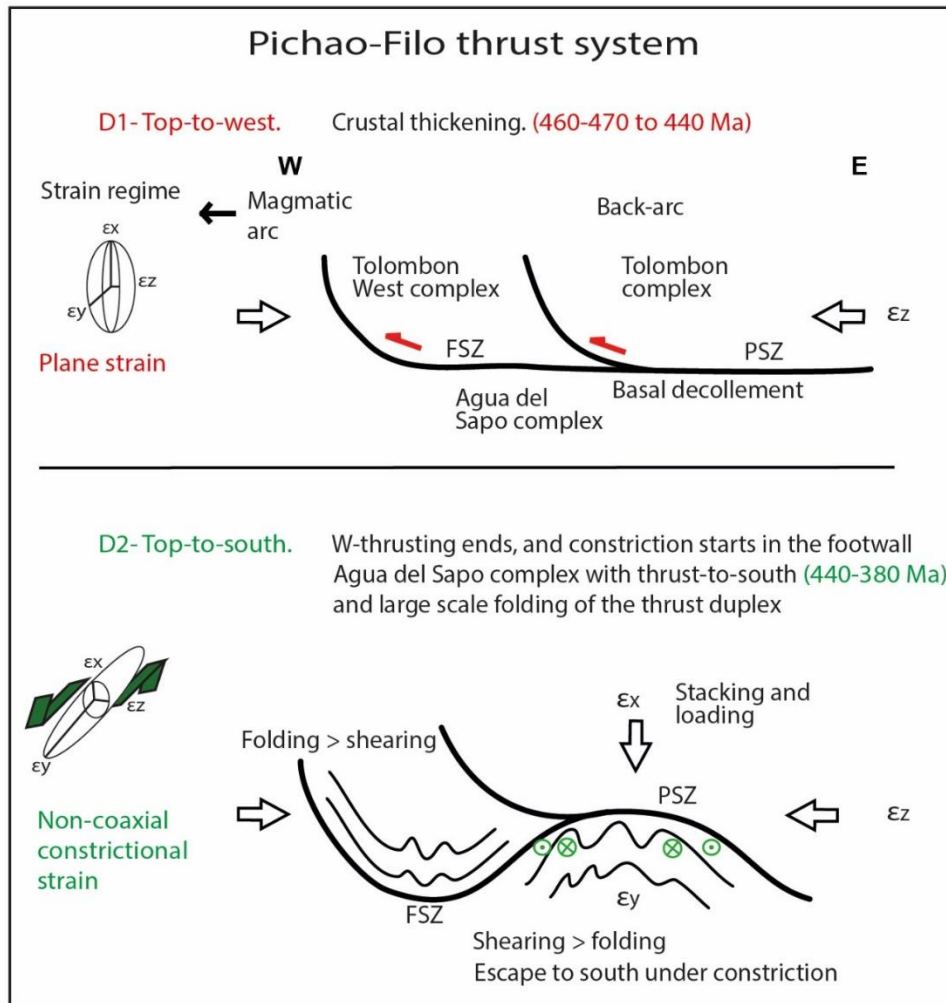
647 5.2 The Pichao-Filo thrust system

648 The geometric arrangement and similarities between the Filo and Pichao Shear Zones (Fig. 2) suggest
649 they formed an interconnected system: (i) they are both wide mylonite-ultramylonite shear zones, (ii)
650 their strain profile is asymmetric, with sharp strain gradient against the Agua del Sapo complex rocks
651 of the footwall and gradational transition towards the hanging wall, and (iii) they have syn-kinematic
652 sillimanite and dynamically recrystallized quartz and Kfs, suggesting high-grade metamorphic
653 conditions of deformation, weakly overprinted by greenschist facies retrogression (Finch et al., 2015).
654 We argue that the Filo Shear Zone together with the eastern section of the Pichao Shear Zone form the
655 basal decollement of a thrust system, and the Tolombon West complex is a horse that is bound by the
656 Filo Shear Zone and the western section of the Pichao Shear Zone (Fig. 12). This system, called here
657 the Pichao-Filo thrust system, placed the Tolombon over the Tolombon West complex, and both were

658 thrusting over the Agua del Sapo complex above the basal decollement during D1. Thrusting led to
659 cooling of the hanging wall rocks that is well-constrained to ~450-440 Ma by the youngest zircon
660 group in Wolfram (2019) and the titanite ages from the Tolombon complex (sample SQ-039 analysed
661 here). In contrast the Agua del Sapo complex footwall remained hot to ~380 Ma (Fig. 10) and
662 continued to be intensely deformed by D2.

663 We envisage that during D2 the basal decollement and the Agua del Sapo footwall were folded
664 upright causing a rotation and steepening of the Filo Shear Zone, as well as its reactivation into a
665 sinistral shear zone, in response to the top-to-south motion (Fig. 12). This reactivation is responsible
666 for the ~7 km sinistral deflection of the Pichao Shear Zone and its overprinting by sub-horizontal
667 stretching lineation in the deflected region. The intense constrictional D2 deformation in the Agua del
668 Sapo complex is presumably because of strain localization to this region that remained hotter than the
669 hanging wall complexes.

670 The evolution of the deformation suggests that D1 lithospheric thickening resulting from westward
671 thrusting perpendicular to the orogen became impeded. This could be a result of the orogen reaching a
672 critical thickness where a balance was reached between the east-west maximum compressional stress
673 and the vertical gravitational stress. Under these conditions, continued east-west shortening led to D2
674 constriction restricted to the warmer footwall complex (Fig. 11). The thrusting to the south during
675 constriction indicates that the lithosphere to the south had not reached the same critical state and that
676 there was still room for thickening allowing for southward lateral escape of the rock mass to fill this
677 gap.



678

679 *Figure 12. Pichao-Filo thrust system, and interpretation of its evolution on cross sections.*
 680 *First, top-to-west thrusting (D1) thickened the crust and transported rocks to the west,*
 681 *towards the magmatic arc. Thrusting then becomes impeded, and stretching parallel to the*
 682 *orogen in a non-coaxial constrictional regime takes over in the thermally weakened Agua del*
 683 *Sapo complex, accompanied by folding and thrusting to the south (D2). During D2, E-W*
 684 *stresses were counterbalanced by vertical stresses and regional force balances lead to*
 685 *southward thrusting in this new constrictional setting.*

686 5.3 Metamorphic conditions during D1 and D2

687 D1 was contemporaneous with anatexis in all three metamorphic complexes. In the Tolombon and
 688 Tolombon West complexes, anatexis was more voluminous than in the Agua del Sapo complex
 689 because of their Al-rich protolith and higher PT conditions. Regardless of that, D1 top-to-west thrusting
 690 and folding in Tolombon and Tolombon West complexes were associated with peak metamorphic
 691 conditions evidenced by leucosomes that are parallel to the S1 axial planar foliation and shear planes
 692 (Figs. 4c and 6a)(Finch et al., 2015; Finch et al., 2016). Similar features are also observed in the Agua
 693 del Sapo complex preserved in the lithons.

694 D2 was also contemporaneous with anatexis in the Tolombon West and Agua del Sapo complexes. In
695 both areas S2 axial planar foliations include biotite and sillimanite (Fig. 4a) and leucosomes are
696 preferentially oriented parallel to S2 (Figs. 4e, 6a, 7c), or in shear zones in the Tolombon West
697 complex. There is also evidence for later undeformed leucosomes cross-cutting deformed metatexites
698 (Fig. 4b, h). Anatexis during D1 and D2 suggests protracted supra-solidus conditions in the Sierra de
699 Quilmes, in accordance with the findings of Wolfram et al. (2019) and further supported by the Zr-in-
700 titanite thermometry (Fig. 10).

701 In the D2 shear zones of the Agua del Sapo complex, the K-feldspar porphyroclasts with core-and-
702 mantle textures and myrmekite are similar to microstructures reported in granitic mylonites that
703 underwent deformation between 450 and 600 °C (Rosenberg and Stünitz, 2003; Tullis and Yund,
704 1991). Quartz shows evidence for sub-grain rotation (SGR) that sometimes progress to an oblique
705 foliation, in the combined SGR and GBM recrystallisation regime (Passchier and Trouw, 2005).
706 These features are overprinted by substantial quartz BLG, and quartz ribbons and aggregates also
707 show recovery to polygonal grains lacking undulose extinction. These features form between ~600 °C
708 (GBM-SGR) and ~400 °C (BLG) and indicate cooling during D2. The Agua del Sapo complex
709 underwent intense muscovitization and muscovite blasts now form mica fish. Muscovitization
710 occurred in both the Agua del Sapo and Tolombon West where D2 has been recorded, but is absent in
711 the Tolombon complex that lacks clear signs of D2. We argue therefore that D2 must have evolved
712 from the higher end of amphibolite facies associated with local anatexis, to the lower end of
713 amphibolite facies with pervasive fluid influx and muscovitization. Muscovitization of the Tolombon
714 West complex gave rise to centimetric grains that are randomly oriented suggesting a late tectonic
715 growth.

716 *Metamorphic conditions of the Filo Shear Zone*

717 The Filo Shear Zone and its splays in the Tolombon West complex preserve grain boundary migration
718 (GBM) in quartz (Fig. 6d), suggesting temperatures above 500 °C (Stipp et al., 2002). This
719 recrystallised quartz have grain-sizes ranging between ~200-400 µm, which is common in mylonite
720 developed at temperatures > 650 °C (Rosenberg and Handy, 2005; Rosenberg and Stünitz, 2003) or >

721 ~550 °C (Stipp et al., 2002). The coexistence of quartz GBM and bulging (BLG) in the same sample
722 (Fig. 6e), suggest also shearing at lower temperatures (~400 °C, Stipp et al., 2002). These
723 temperatures only provide broad constraints as the recrystallisation mechanism is strongly influenced
724 by the presence of fluids, differential stress, and variable strain rate (Law, 2014; Passchier and Trouw,
725 2005). Better constraints are provided by the stable paragenesis. This includes syn-kinematic
726 sillimanite suggesting shearing at upper amphibolite facies conditions (Büttner et al., 2005; Larrovere
727 et al., 2008), while the presence of epidote with allanite cores in Ca-rich mylonitic rocks are stable
728 below 700-750 °C (Budzyń et al., 2017; Janots et al., 2008; Wing et al., 2003). Combining quartz
729 microstructures and mineral paragenesis, we estimate that the Filo Shear Zone developed at
730 amphibolite facies conditions with temperatures between 700 and 550 °C, and was overprinted at
731 ~400 °C as evidenced by the BLG of quartz and weak chloritization of the stable mineralogy. The
732 latter was probably a low-intensity deformation, insufficient to erase the GBM features.

733 5.4 Timing of D2

734 Titanite dates in the Tolombon complex, between 475-440 Ma (Fig. 10a) compare with monazite and
735 zircon dates between ~505-440 Ma (Finch et al., 2017; Weinberg et al., 2020; Wolfram et al., 2019).
736 All three geochronometres closed their isotopic systems at ~440 Ma, inferred to date the cooling
737 resulting from exhumation related to D1 thrusting (Finch et al., 2017). Given that shortening in the
738 Famatinian orogeny started between 470 to 460 Ma (Weinberg et al., 2019), it is likely that D1 took
739 place between 470-460 Ma and ~440 Ma.

740 Unlike the Tolombon complex, the Agua del Sapo complex remained hot for longer (Fig. 10). Finch
741 et al. (2017) reported monazite U-Pb ages from two samples from the Agua del Sapo complex.
742 Monazite from a schist in the immediate footwall of the PSZ (SQ84a) yielded dates that range
743 between 490-450 Ma, similar to those of the hanging wall. The other sample, from ~1 km further
744 south (SQ181a), yielded dates between 435-420 Ma. These two date groups are reflected in our
745 titanite dates in Fig. 10, with some samples yielding dates between ~500 and 440 Ma, and others
746 between ~440 and ~380 Ma.

747 The entire 120 Ma range recorded by titanite in the Agua del Sapo complex, from 500 to 380 Ma, is
748 associated with Zr-in-titanite temperatures between ~750-700 °C, peaking at ~460 Ma and cooling
749 gently thereafter (Fig. 10b). This suggests that the footwall of the Pichao-Filo thrusts remained at or
750 above 700 °C some 60 Ma longer than the hanging wall, undergoing a very slow cooling during this
751 period, at rates of ~1 °C/Ma. The growth of monazite and titanite in the footwall after 440 Ma was
752 likely assisted by both sustained high temperatures and shearing. Lucassen (2003) reported a similar
753 case to the west of the Sierra de Quilmes, in another Famatinian migmatitic terrane, where
754 deformation-enhanced recrystallization of titanite at temperature > 650 °C resulted in a semi-
755 continuous titanite formation between 470-420 Ma (see also (Gasser et al., 2015) for protracted
756 titanite formation). A remaining question is why did titanite from different samples record different
757 periods of the metamorphic history when the samples have similar mineralogical and structural
758 makeup? The answer could be related to different mineral reactivity related to small compositional
759 differences between samples, or variable distribution of deformation and/or fluids (Cherniak et al.,
760 2004; Harlov and Hetherington, 2010; Schoene, 2014; Taylor et al., 2016).

761 5.5 Sustained high-temperatures and the origin of D2

762 Back-arc terranes, such as that of the Famatinian Orogen, are wide, hot and rheologically weak parts
763 of the crust (Hyndman et al., 2005). They are therefore susceptible to take up deformation. During
764 shortening, back-arcs may be too weak to build up a thick crust and are instead prone to lateral and
765 transversal spread (Beaumont et al., 2010; Cruden et al., 2006; Jamieson and Beaumont, 2013)
766 maintaining a subdued topography. The magnitude of this flow depends on the balance between
767 crustal thickening and gravity-driven extension (Jamieson et al., 2011), and modulated by partial
768 melting (Vanderhaeghe, 2009; Vanderhaeghe and Teyssier, 2001). Hot orogens where lateral flow
769 leads to a subdued topography will form plateaus underlain by a weak ductile crust. A classic example
770 of this is the thermally softened Variscan orogen that Franke et al. (2014) described as a “failed”
771 orogen, unfit for stacking.

772 The protracted high-temperature conditions in Sierra de Quilmes with evidence for multiple melting
773 events (Wolfram et al., 2019), suggests that heat was inherited from the early extensional phase that

774 lasted from ca. 500 to 470-460 Ma (Weinberg et al., 2018), and sustained long-term by a combination
775 of modest crustal thickening of a heat producing crust and intense heat flow from the mantle
776 (Wolfram et al., 2017). The switch at 470-460 Ma, from extension to the shortening phase started the
777 Oclóyic phase resulting in both D1 and D2 events.

778 In summary, the Sierra de Quilmes exposes the mid-crustal section of the thermally-mature
779 Famatinian continental back-arc that during the Oclóyic phase evolved from a stage of thickening
780 (D1), where the three HT-LP complexes were stacked forming a large thrust duplex, to a stage of
781 southward thrusting and N-S stretching (D2). D1 lasted from 470-460 Ma and ended at ~440 Ma
782 when thrust-to-west was impeded and D2 started. The colder hanging wall complexes were little
783 affected by D2, with only folding and minor shearing recorded in the Tolombon West complex.
784 Intense deformation with constriction and top-to-south thrusting was restricted to the hot Agua del
785 Sapo footwall. D2 can be explained by a regional imbalance of the vertical forces that caused a lateral
786 pressure gradient. We postulate that lithospheric thickening during D1 was more intense to the north
787 driving material escape to the south during D2.

788 6 Conclusion

789 The Sierra de Quilmes records two major deformational events that occurred during the shortening
790 Oclóyic phase of the Famatinian orogenic cycle. The first event, D1, is characterised by a high-
791 temperature syn-anatectic thrust-to-the-west, forming the Pichao-Filo thrust system and a large-scale
792 duplex structure. Lithospheric thickening as a result of D1 reached a critical point in which further
793 thrusting was impeded. At this point D2 started, characterized by constriction with a N-S stretching
794 direction, and N-S doubly plunging folds and thrusting to the south, parallel to the orogen. While this
795 event did not affect the hanging wall Tolombon complex, it led to syn-anatectic folding in the
796 Tolombon West complex, and intense, syn-anatectic shearing in the Agua del Sapo complex, the
797 footwall of the duplex. The latter was strongly stretched, folded and thrust in this non-coaxial
798 constrictional event. The deformation history was therefore characterized by a continuous,
799 unidirectional east-west convergence that evolved from thrusting perpendicular to the orogen from
800 470-460 to ~440 Ma, to thrusting parallel to the orogen thereafter, driven by lateral variations in

801 lithospheric thicknesses. Titanite geochronology and geothermometry suggest that the footwall
802 remained hot and structurally active between ~440 possibly to 380 Ma, long after the hanging wall
803 had cooled and ceased deforming. In summary, the Oclóyic phase of the Famatinian orogen gave rise
804 to a long-lived, wide and hot orogen that was too weak to sustain high topography, forcing the
805 orogenic edifice to spread laterally similar to the thermally weakened Grenvillian or Variscan orogens
806 (Beaumont et al., 2010; Jamieson and Beaumont, 2013), and the mid-crustal sections of the
807 Himalayan (Parsons et al., 2016).

808 **Acknowledgements**

809 We thank David Kelsey for the comments and discussion that improved significantly this
810 manuscript. We thank also colleagues⁴⁹ from the Universidad de Salta, Nestor Suzaño, Agustin Ortiz
811 and Alexis Nieves for the discussions and support in the extraordinary field trips. This research was
812 supported by the Australian Research Council grant no. DP110102543 (to R.F.W.).

813 Datasets for this research are available at Monash University repository:

814 <https://figshare.com/s/5ed9fc54d98be2e32ff2>

815

816 References

817

818

819 Aceñolaza, F. G., Miller, H., and Toselli, A. J., 2002, Proterozoic - Early Paleozoic evolution in western
820 South America - A discussion: *Tectonophysics*, v. 354, p. 121-137.

821 Adams, C. J., Miller, H., Aceñolaza, F. G., Toselli, A. J., and Griffin, W. L., 2011, The Pacific Gondwana
822 margin in the late Neoproterozoic–early Paleozoic: Detrital zircon U–Pb ages from
823 metasediments in northwest Argentina reveal their maximum age, provenance and tectonic
824 setting: *Gondwana Research*, v. 19, p. 71-83.

825 Aleinikoff, J. N., Wintsch, R. P., Tollo, R. P., Unruh, D. M., Fanning, C. M., and Schmitz, M. D., 2007,
826 Ages and origins of rocks of the Killingworth dome, south-central Connecticut: Implications
827 for the tectonic evolution of southern New England: *American Journal of Science*, v. 307, p.
828 63-118.

829 Astini, R., 2008, Sedimentación, facies, discordancias y evolución paleoambiental durante el Cambro-
830 Ordovícico, *Revista de la Asociación Geológica Argentina*, 50-73 p.

831 Astini, R. A., 1998, Stratigraphical evidence supporting the rifting, drifting and collision of the
832 Laurentian Precordillera terrane of western Argentina, *The Geological Society*, v. 142, p. 11-
833 33.

834 Astini, R. A., and Dávila, F. M., 2004, Ordovician back arc foreland and Oclöyic thrust belt
835 development on the western Gondwana margin as a response to Precordillera terrane
836 accretion: *Tectonics*, v. 23, p. TC4008 1-19.

837 Bahlburg, H., Berndt, J., and Gerdes, A., 2016, The ages and tectonic setting of the Faja Eruptiva de
838 la Puna Oriental, Ordovician, NW Argentina: *Lithos*, v. 256-257, p. 41-54.

839 Bahlburg, H., and Breitzkreuz, C., 1991, Paleozoic evolution of active margin basins in the southern
840 Central Andes (northwestern Argentina and northern Chile): *Journal of South American
841 Earth Sciences*, v. 4, p. 171-188.

842 Bahlburg, H., and Hervé, F., 1997a, Geodynamic evolution and tectonostratigraphic terranes of
843 northwestern Argentina and northern Chile: *Bulletin of the Geological Society of America*, v.
844 109, p. 869-884.

845 Bahlburg, H., and Hervé, F., 1997b, Geodynamic evolution and tectonostratigraphic terranes of
846 northwestern Argentina and northern Chile: *Geological Society of America Bulletin*, v. 109, p.
847 869-884.

848 Beaumont, C., Jamieson, R., and Nguyen, M., 2010, Models of large, hot orogens containing a
849 collage of reworked and accreted terranes: *Canadian Journal of Earth Sciences*, v. 47, p. 485-
850 515.

851 Bons, P. D., Jansen, D., Mundel, F., Bauer, C. C., Binder, T., Eisen, O., Jessell, M. W., Llorens, M. G.,
852 Steinbach, F., Steinhage, D., and Weikusat, I., 2016, Converging flow and anisotropy cause
853 large-scale folding in Greenland's ice sheet: *Nature Communications*, v. 7.

854 Braathen, A., Nordgulen, O., Osmundsen, P. T., Andersen, T. B., Solli, A., and Roberts, D., 2000,
855 Devonian, orogen-parallel, opposed extension in the Central Norwegian Caledonides:
856 *Geology*, v. 28, p. 615-618.

857 Budzyń, B., Harlov, D. E., Kozub-Budzyń, G. A., and Majka, J., 2017, Experimental constraints on the
858 relative stabilities of the two systems monazite-(Ce) – allanite-(Ce) – fluorapatite and

- 859 xenotime-(Y) – (Y,HREE)-rich epidote – (Y,HREE)-rich fluorapatite, in high Ca and Na-Ca
860 environments under P-T conditions of 200–1000 MPa and 450–750 °C: *Mineralogy and*
861 *Petrology*, v. 111, p. 183-217.
- 862 Büttner, S. H., 2009, The Ordovician Sierras Pampeanas–Puna basin connection: Basement thinning
863 and basin formation in the Proto-Andean back-arc: *Tectonophysics*, v. 477, p. 278-291.
- 864 Büttner, S. H., Glodny, J., Lucassen, F., Wemmer, K., Erdmann, S., Handler, R., and Franz, G., 2005,
865 Ordovician metamorphism and plutonism in the Sierra de Quilmes metamorphic complex:
866 Implications for the tectonic setting of the northern Sierras Pampeanas (NW Argentina):
867 *Lithos*, v. 83, p. 143-181.
- 868 Carreras, J., Cosgrove, J. W., and Druguet, E., 2013, Strain partitioning in banded and/or anisotropic
869 rocks: Implications for inferring tectonic regimes: *Journal of Structural Geology*, v. 50, p. 7-
870 21.
- 871 Cawood, P. A., 2005, Terra Australis Orogen: Rodinia breakup and development of the Pacific and
872 Iapetus margins of Gondwana during the Neoproterozoic and Paleozoic: *Earth-Science*
873 *Reviews*, v. 69, p. 249-279.
- 874 Chambers, J. A., and Kohn, M. J., 2012, Titanium in muscovite, biotite, and hornblende: Modeling,
875 thermometry, and rutile activities of metapelites and amphibolites: *American Mineralogist*,
876 v. 97, p. 543-555.
- 877 Chardon, D., Gapais, D., and Cagnard, F., 2009, Flow of ultra-hot orogens: A view from the
878 Precambrian, clues for the Phanerozoic: *Tectonophysics*, v. 477, p. 105-118.
- 879 Chardon, D., and Jayananda, M., 2008, Three-dimensional field perspective on deformation, flow,
880 and growth of the lower continental crust (Dharwar craton, India): *Tectonics*, v. 27.
- 881 Chardon, D., Jayananda, M., and Peucat, J.-J., 2011, Lateral constrictional flow of hot orogenic crust:
882 Insights from the Neoproterozoic of south India, geological and geophysical implications for
883 orogenic plateaux: *Geochemistry Geophysics Geosystems - GEOCHEM GEOPHYS GEOSYST*, v.
884 12.
- 885 Cherniak, D. J., Watson, E. B., Grove, M., and Harrison, T. M., 2004, Pb diffusion in monazite: A
886 combined RBS/SIMS study: *Geochimica et Cosmochimica Acta*, v. 68, p. 829-840.
- 887 Collins, W. J., 2002, Hot orogens, tectonic switching, and creation of continental crust: *Geology*, v.
888 30, p. 535-538.
- 889 Cruden, A. R., Nasser, M. H. B., and Pysklywec, R., 2006, Surface topography and internal strain
890 variation in wide hot orogens from three-dimensional analogue and two-dimensional
891 numerical vice models, *Geological Society Special Publication*, 253, p. 79-104.
- 892 Curie, C. A., and Hyndman, R. D., 2006, The thermal structure of subduction zone back arcs: *Journal*
893 *of Geophysical Research: Solid Earth*, v. 111.
- 894 Davila, F. M., Astini, R. A., and Schmidt, C. J., 2003, Unraveling 470 m.y. of shortening in the Central
895 Andes and documentation of Type O superposed folding: *Geology*, v. 31, p. 275-278.
- 896 Escayola, M. P., van Staal, C. R., and Davis, W. J., 2011, The age and tectonic setting of the
897 Puncoviscana Formation in northwestern Argentina: An accretionary complex related to
898 Early Cambrian closure of the Puncoviscana Ocean and accretion of the Arequipa-Antofalla
899 block: *Journal of South American Earth Sciences*, v. 32, p. 438-459.
- 900 Finch, M. A., Weinberg, R. F., Fuentes, M. G., Hasalová, P., and Becchio, R., 2015, One kilometre-
901 thick ultramylonite, Sierra de Quilmes, Sierras Pampeanas, NW Argentina: *Journal of*
902 *Structural Geology*, v. 72, p. 33-54.
- 903 Finch, M. A., Weinberg, R. F., Hasalová, P., Becchio, R., Fuentes, M. G., and Kennedy, A., 2017,
904 Tectono-metamorphic evolution of a convergent back-arc: The Famatinian orogen, Sierra de

- 905 Quilmes, Sierras Pampeanas, NW Argentina: *Bulletin of the Geological Society of America*, v.
906 129, p. 1602–1621.
- 907 Finch, M. A., Weinberg, R. F., and Hunter, N. J. R., 2016, Water loss and the origin of thick
908 ultramylonites: *Geology*, v. 44, p. 599-602.
- 909 Fletcher, J. M., and Bartley, J. M., 1994, Constrictional strain in a non-coaxial shear zone:
910 implications for fold and rock fabric development, central mojave metamorphic core
911 complex, california: *Journal of Structural Geology*, v. 16, p. 555-570.
- 912 Franke, W., 2014, Topography of the Variscan orogen in Europe: Failed-not collapsed: *International
913 Journal of Earth Sciences*, v. 103, p. 1471-1499.
- 914 Gasser, D., Jeřábek, P., Faber, C., Stünitz, H., Menegon, L., Corfu, F., Erambert, M., and Whitehouse,
915 M. J., 2015, Behaviour of geochronometers and timing of metamorphic reactions during
916 deformation at lower crustal conditions: Phase equilibrium modelling and U-Pb dating of
917 zircon, monazite, rutile and titanite from the Kalak Nappe Complex, northern Norway:
918 *Journal of Metamorphic Geology*, v. 33, p. 513-534.
- 919 Hajná, J., Žák, J., Kachlík, V., and Chadima, M., 2012, Deciphering the Variscan tectonothermal
920 overprint and deformation partitioning in the Cadomian basement of the Teplá-Barrandian
921 unit, Bohemian Massif: *International Journal of Earth Sciences*, v. 101, p. 1855-1873.
- 922 Harlov, D. E., and Hetherington, C. J., 2010, Partial high-grade alteration of monazite using alkali-
923 bearing fluids: Experiment and nature: *American Mineralogist*, v. 95, p. 1105-1108.
- 924 Hayden, L. A., Watson, E. B., and Wark, D. A., 2008, A thermobarometer for sphene (titanite):
925 *Contributions to Mineralogy and Petrology*, v. 155, p. 529-540.
- 926 Heilbronner, R., and Tullis, J., 2006, Evolution of c axis pole figures and grain size during dynamic
927 recrystallization: Results from experimentally sheared quartzite: *Journal of Geophysical
928 Research: Solid Earth*, v. 111.
- 929 Heuret, A., Funicello, F., Faccenna, C., and Lallemand, S., 2007, Plate kinematics, slab shape and
930 back-arc stress: A comparison between laboratory models and current subduction zones:
931 *Earth and Planetary Science Letters*, v. 256, p. 473-483.
- 932 Heuret, A., and Lallemand, S., 2005, Plate motions, slab dynamics and back-arc deformation: *Physics
933 of the Earth and Planetary Interiors*, v. 149, p. 31-51.
- 934 Horstwood, M. S. A., Košler, J., Gehrels, G., Jackson, S. E., McLean, N. M., Paton, C., Pearson, N. J.,
935 Sircombe, K., Sylvester, P., Vermeesch, P., Bowring, J. F., Condon, D. J., and Schoene, B.,
936 2016, Community-Derived Standards for LA-ICP-MS U-(Th-)Pb Geochronology – Uncertainty
937 Propagation, Age Interpretation and Data Reporting: *Geostandards and Geoanalytical
938 Research*, v. 40, p. 311-332.
- 939 Hunter, N. J. R., Hasalová, P., Weinberg, R. F., and Wilson, C. J. L., 2016, Fabric controls on strain
940 accommodation in naturally deformed mylonites: The influence of interconnected
941 micaceous layers: *Journal of Structural Geology*, v. 83, p. 180-193.
- 942 Hyndman, R. D., Currie, C. A., and Mazzotti, S. P., 2005, Subduction zone backarcs, mobile belts, and
943 orogenic heat: *GSA Today*, v. 15, p. 4-10.
- 944 Jamieson, R. A., and Beaumont, C., 2013, On the origin of orogens: *Bulletin of the Geological Society
945 of America*, v. 125, p. 1671-1702.
- 946 Jamieson, R. A., Unsworth, M. J., Harris, N. B. W., Rosenberg, C. L., and Schulmann, K., 2011, Crustal
947 melting and the flow of mountains: *Elements*, v. 7, p. 253-260.
- 948 Janots, E., Engi, M., Berger, A., Allaz, J., Schwarz, J. O., and Spandler, C., 2008, Prograde
949 metamorphic sequence of REE minerals in pelitic rocks of the Central Alps: Implications for

- 950 allanite-monazite-xenotime phase relations from 250 to 610°C: *Journal of Metamorphic*
951 *Geology*, v. 26, p. 509-526.
- 952 Jolivet, L., Famin, V., Mehl, C., Parra, T., Aubourg, C., Hébert, R., and Philippot, P., 2004, Strain
953 localization during crustal-scale boudinage to form extensional metamorphic domes in the
954 Aegean Sea: *Geological Society of America Special Paper* 380, p. 185-210.
- 955 Kapp, P., Manning, C. E., and Tropper, P., 2009, Phase-equilibrium constraints on titanite and rutile
956 activities in mafic epidote amphibolites and geobarometry using titanite-rutile equilibria:
957 *Journal of Metamorphic Geology*, v. 27, p. 509-521.
- 958 Kennedy, A. K., Kamo, S. L., Nasdala, L., and Timms, N. E., 2010, Grenville skarn titanite: Potential
959 reference material for SIMS U-Th-Pb analysis: *Canadian Mineralogist*, v. 48, p. 1423-1443.
- 960 Kilian, R., Heilbronner, R., and Stünitz, H., 2011, Quartz grain size reduction in a granitoid rock and
961 the transition from dislocation to diffusion creep: *Journal of Structural Geology*, v. 33, p.
962 1265-1284.
- 963 Kohn, M. J., 2017, Titanite Petrochronology: *Reviews in Mineralogy and Geochemistry*, v. 83, p. 419-
964 441.
- 965 Larrovere, M. A., Alasino, P. H., and Baldo, E. G., 2016, The double-vergent ductile shear zone of
966 northwestern Sierra de Velasco: Deformation of the middle crust during the Famatinian
967 orogeny: *Revista de la Asociación Geológica Argentina*, v. 73, p. 117-133.
- 968 Larrovere, M. A., de los Hoyos, C. R., Toselli, A. J., Rossi, J. N., Basei, M. A. S., and Belmar, M. E.,
969 2011, High T/P evolution and metamorphic ages of the migmatitic basement of northern
970 Sierras Pampeanas, Argentina: Characterization of a mid-crustal segment of the Famatinian
971 belt: *Journal of South American Earth Sciences*, v. 31, p. 279-297.
- 972 Larrovere, M. A., Toselli, A., and Rossi De Toselli, J. N., 2008, Petrology and structure of La Chilca
973 Shear Zone, Catamarca: *Revista de la Asociación Geológica Argentina*, v. 63, p. 254-263.
- 974 Law, R. D., 2014, Deformation thermometry based on quartz c-axis fabrics and recrystallization
975 microstructures: A review: *Journal of Structural Geology*, v. 66, p. 129-161.
- 976 Lister, G., and Forster, M., 2009, Tectonic mode switches and the nature of orogenesis: *Lithos*, v.
977 113, p. 274-291.
- 978 Lister, G. S., and Hobbs, B. E., 1980, The simulation of fabric development during plastic
979 deformation and its application to quartzite: the influence of deformation history: *Journal of*
980 *Structural Geology*, v. 2, p. 355-370.
- 981 Lucassen, F., and Becchio, R., 2003, Timing of high-grade metamorphism: Early Palaeozoic U-Pb
982 formation ages of titanite indicate long-standing high-T conditions at the western margin of
983 Gondwana (Argentina, 26-29°S): *Journal of Metamorphic Geology*, v. 21, p. 649-662.
- 984 Malavieille, J., 1993, Late Orogenic extension in mountain belts: Insights from the basin and range
985 and the Late Paleozoic Variscan Belt: *Tectonics*, v. 12, p. 1115-1130.
- 986 Mancktelow, N. S., and Pavlis, T. L., 1994, Fold-fault relationships in low-angle detachment systems:
987 *Tectonics*, v. 13, p. 668-685.
- 988 Moya, M., 2015, La Fase Oclóyica (Ordovícico Superior) en el noroeste argentino. Interpretación
989 histórica y evidencias en contrario: *Serie Correlación Geológica*, v. 3, p. 73-110.
- 990 Mulcahy, S. R., Roeske, S. M., McClelland, W. C., Ellis, J. R., Jourdan, F., Renne, P. R., Vervoort, J. D.,
991 and Vujovich, G. I., 2014, Multiple migmatite events and cooling from granulite facies
992 metamorphism within the Famatina arc margin of northwest Argentina: *Tectonics*, v. 33, p.
993 1-25.

- 994 Omarini, R. H., Sureda, R. J., Götze, H. J., Seilacher, A., and Pflüger, F., 1999, Puncoviscana folded
995 belt in northwestern Argentina: Testimony of Late Proterozoic Rodinia fragmentation and
996 pre-Gondwana collisional episodes: *International Journal of Earth Sciences*, v. 88, p. 76-97.
- 997 Ortiz, A., Suzaño, N., Hauser, N., Becchio, R., and Nieves, A., 2019, New hints on the evolution of the
998 Eastern Magmatic Belt, Puna Argentina. SW Gondwana margin: Zircon U-Pb ages and Hf
999 isotopes in the Pachamama Igneous-Metamorphic Complex: *Journal of South American
1000 Earth Sciences*, v. 94, p. 102246.
- 1001 Parsons, A. J., Ferré, E. C., Law, R. D., Lloyd, G. E., Phillips, R. J., and Searle, M. P., 2016, Orogen-
1002 parallel deformation of the Himalayan midcrust: Insights from structural and magnetic fabric
1003 analyses of the Greater Himalayan Sequence, Annapurna-Dhaulagiri Himalaya, central
1004 Nepal: *Tectonics*, v. 35, p. 2515-2537.
- 1005 Passchier, C. W., and Trouw, R. A. J., 2005, *Microtectonics*, Springer Berlin Heidelberg, 1-366 p.
- 1006 Pennacchioni, G., Menegon, L., Leiss, B., Nestola, F., and Bromiley, G., 2010, Development of
1007 crystallographic preferred orientation and microstructure during plastic deformation of
1008 natural coarse-grained quartz veins: *Journal of Geophysical Research: Solid Earth*, v. 115.
- 1009 Peterzell, M., Hasalová, P., Wilson, C. J. L., Piazzolo, S., and Schulmann, K., 2010, Evaluating quartz
1010 crystallographic preferred orientations and the role of deformation partitioning using EBSD
1011 and fabric analyser techniques: *Journal of Structural Geology*, v. 32, p. 803-817.
- 1012 Piñán-Llamas, A., and Simpson, C., 2009, Primary structure influence on compositional banding in
1013 psammites: Examples from the Puncoviscana Formation, north-central Argentina: *Journal of
1014 Structural Geology*, v. 31, p. 55-71.
- 1015 Ramos, V. A., 2008, The basement of the Central Andes: The arequipa and related terranes, *in*
1016 Jeanloz, R., Albee, A. L., Burke, K. C., and Freeman, K. H., eds., *Annual Review of Earth and
1017 Planetary Sciences*, 36, p. 289-324.
- 1018 Ramos, V. A., 2009, Anatomy and global context of the Andes: Main geologic features and the
1019 Andean orogenic cycle, *Memoir of the Geological Society of America*, 204, p. 31-65.
- 1020 Ramos, V. A., Dallmeyer, R. D., and Vujovich, G., 1998, Time constraints on the Early Palaeozoic
1021 docking of the Precordillera, central Argentina, *Geological Society Special Publication*, 142, p.
1022 143-158.
- 1023 Ramos, V. A., Escayola, M., Mutti, D. I., and Vujovich, G. I., 2000, Proterozoic-early Paleozoic
1024 ophiolites of the Andean basement of southern South America, *Special Paper of the
1025 Geological Society of America*, 349, p. 331-349.
- 1026 Ramos, V. A., Jordan, T. E., Allmendinger, R. W., Mpodozis, C., Kay, S. M., Cortés, J. M., and Palma,
1027 M., 1986, Paleozoic terranes of the central Argentine-Chilean Andes: *Tectonics*, v. 5, p. 855-
1028 880.
- 1029 Ramsay, J. G., and Huber, M. I., 1983, *The techniques of modern structural geology. Volume 1:
1030 strain analysis: The techniques of modern structural geology. Volume 1: strain analysis.*
- 1031 Rapela, C., Pankhurst, R., Casquet, C., A. Dahlquist, J., Mark Fanning, C., G. Baldo, E., Galindo, C.,
1032 Alasino, P., Ramacciotti, C., Verdecchia, S., Murra, J., and Basei, M., 2018, A review of the
1033 Famatinian Ordovician magmatism in southern South America: Evidence of lithosphere
1034 reworking and continental subduction in the early proto-Andean margin of Gondwana:
1035 *Earth-Science Reviews*, v. 187, p. 259-285.
- 1036 Rapela, C. W., 1976, El Basamento Metamorfico de la Region de Cafayate, Provincia de Salta.
1037 Aspectos Petrologicos y Geoquimicos: *Revista de la Asociacion Geologica Argentina*, v. 3, p.
1038 203-222.

- 1039 Rapela, C. W., Pankhurst, R. J., Casquet, C., Baldo, E., Saavedra, J., Galindo, C., and Fanning, C. M.,
1040 1998a, The Pampean Orogeny of the southern proto-Andes: Cambrian continental collision
1041 in the Sierras de Cordoba: Geological Society, London, Special Publications, v. 142, p. 181-
1042 217.
- 1043 Rapela, C. W., Pankhurst, R. J., Saavedra, J., and Galindo, C., 1998b, Early evolution of the proto-
1044 andean margin of South America: *Geology*, v. 26, p. 707-710.
- 1045 Rapela, C. W., Verdecchia, S. O., Casquet, C., Pankhurst, R. J., Baldo, E. G., Galindo, C., Murra, J. A.,
1046 Dahlquist, J. A., and Fanning, C. M., 2015, Identifying Laurentian and SW Gondwana sources
1047 in the Neoproterozoic to Early Paleozoic metasedimentary rocks of the Sierras Pampeanas:
1048 Paleogeographic and tectonic implications: *Gondwana Research*, v. 32, p. 193-212.
- 1049 Rosenberg, C. L., and Handy, M. R., 2005, Experimental deformation of partially melted granite
1050 revisited: Implications for the continental crust: *Journal of Metamorphic Geology*, v. 23, p.
1051 19-28.
- 1052 Rosenberg, C. L., and Stünitz, H., 2003, Deformation and recrystallization of plagioclase along a
1053 temperature gradient: An example from the Bergell tonalite: *Journal of Structural Geology*,
1054 v. 25, p. 389-408.
- 1055 Rossi, J., and Toselli, A., 1976, Migmatization y Metamorfismo en el basamento de la Sierra de
1056 Quilmes, al Oeste de Colalao del Valle, Tucuman: *Revista de la Asociacion Geologica*
1057 Argentina, v. 2, p. 83-94.
- 1058 Rubio Pascual, F. J., López-Carmona, A., and Arenas, R., 2016, Thickening vs. extension in the
1059 Variscan belt: P–T modelling in the Central Iberian autochthon: *Tectonophysics*, v. 681, p.
1060 144-158.
- 1061 Sawyer, E. W., 2008, *Atlas of Migmatites*, NRC Research Press and Mineralogical Association of
1062 Canada, 387 p.
- 1063 Schoene, B., 2014, 4.10 - U–Th–Pb Geochronology, *in* Holland, H. D., and Turekian, K. K., eds.,
1064 *Treatise on Geochemistry (Second Edition)*: Oxford, Elsevier, p. 341-378.
- 1065 Schoene, B., Condon, D. J., Morgan, L., and McLean, N., 2013, Precision and accuracy in
1066 geochronology: *Elements*, v. 9, p. 19-24.
- 1067 Schwartz, J. J., Gromet, L. P., and Miro, R., 2008, Timing and Duration of the Calc-Alkaline Arc of the
1068 Pampean Orogeny: Implications for the Late Neoproterozoic to Cambrian Evolution of
1069 Western Gondwana: *The Journal of Geology*, v. 116, p. 39-61.
- 1070 Semenov, I., Weinberg, R., Taylor, R., and Jourdan, F., 2019, Prolonged Movement on a > 10-km-
1071 Wide Thrust During Early Paleozoic Orogens in the Gondwana Margin of NW Argentina:
1072 *Tectonics*.
- 1073 Semenov, I., and Weinberg, R. F., 2017, A major mid-crustal decollement of the Paleozoic
1074 convergent margin of western Gondwana: The Guacha Corral shear zone, Argentina: *Journal*
1075 *of Structural Geology*, v. 103, p. 75-99.
- 1076 Skjerna, L., 1989, Tubular folds and sheath folds: definitions and conceptual models for their
1077 development, with examples from the Grapesvare area, northern Sweden: *Journal of*
1078 *Structural Geology*, v. 11, p. 689-703.
- 1079 Sola, A. M., Becchio, R. A., and Pimentel, M. M., 2013, Petrogenesis of migmatites and leucogranites
1080 from Sierra de Molinos, Salta, Northwest Argentina: A petrologic and geochemical study:
1081 *Lithos*, v. 177, p. 470-491.
- 1082 Sola, A. M., Hasalová, P., Weinberg, R. F., Suzaño, N. O., Becchio, R. A., Hongn, F. D., and Botelho, N.,
1083 2017, Low-P melting of metapelitic rocks and the role of H₂O: Insights from phase equilibria
1084 modelling: *Journal of Metamorphic Geology*, v. 35, p. 1131-1159.

- 1085 Stacey, J. S., and Kramers, J., 1975, Approximation of Terrestrial Lead Isotope Evolution by a 2-Stage
1086 Model: *Earth and Planetary Science Letters*, v. 26, p. 207-221.
- 1087 Stipp, M., Stünitz, H., Heilbronner, R., and Schmid, S. M., 2002, The eastern Tonale fault zone: A
1088 'natural laboratory' for crystal plastic deformation of quartz over a temperature range from
1089 250 to 700 °C: *Journal of Structural Geology*, v. 24, p. 1861-1884.
- 1090 Sullivan, W. A., 2009, Kinematic significance of L tectonites in the footwall of a major terrane-
1091 bounding thrust fault, Klamath Mountains, California, USA: *Journal of Structural Geology*, v.
1092 31, p. 1197-1211.
- 1093 Sullivan, W. A., 2013, L tectonites: *Journal of Structural Geology*, v. 50, p. 161-175.
- 1094 Sullivan, W. A., and Beane, R. J., 2010, Asymmetrical quartz crystallographic fabrics formed during
1095 constrictional deformation: *Journal of Structural Geology*, v. 32, p. 1430-1443.
- 1096 Sullivan, W. A., and Law, R. D., 2007, Deformation path partitioning within the transpressional
1097 White Mountain shear zone, California and Nevada: *Journal of Structural Geology*, v. 29, p.
1098 583-599.
- 1099 Taylor, R. J. M., Kirkland, C. L., and Clark, C., 2016, Accessories after the facts: Constraining the
1100 timing, duration and conditions of high-temperature metamorphic processes: *Lithos*, v. 264,
1101 p. 239-257.
- 1102 Thomas, W. A., and Astini, R. A., 2003, Ordovician accretion of the Argentine Precordillera terrane
1103 to Gondwana: A review: *Journal of South American Earth Sciences*, v. 16, p. 67-79.
- 1104 Toselli, A., Rossi, J., and Rapela, C. W., 1978, El Basamento Metamorfico de la Sierra de Quilmes,
1105 Republica Argentina: *Revista de la Asociacion Geologica Argentina*, v. 33, p. 105-121.
- 1106 Tullis, J., and Yund, R. A., 1991, Diffusion creep in feldspar aggregates: experimental evidence:
1107 *Journal of Structural Geology*, v. 13, p. 987-1000.
- 1108 Turner, J. C. M., 1975, Geología del sector oriental de los Departamentos de Santa Victoria e Iruya,
1109 Provincia de Salta. República Argentina: *Boletín de la Academia Nacional de Ciencias: Boletín*
1110 *de la Academia Nacional de Ciencias*, v. 51, p. 11-24.
- 1111 Vanderhaeghe, O., 2009, Migmatites, granites and orogeny: Flow modes of partially-molten rocks
1112 and magmas associated with melt/solid segregation in orogenic belts: *Tectonophysics*, v.
1113 477, p. 119-134.
- 1114 Vanderhaeghe, O., and Teyssier, C., 2001, Partial melting and flow of orogens: *Tectonophysics*, v.
1115 342, p. 451-472.
- 1116 Weinberg, R. F., Becchio, R., Farias, P., Suzaño, N., and Sola, A., 2018b, Early Paleozoic accretionary
1117 orogenies in NW Argentina: Growth of West Gondwana: *Earth-Science Reviews*, v. 187, p.
1118 219-247.
- 1119 Weinberg, R. F., Wolfram, L. C., Nebel, O., Hasalová, P., Závada, P., Kylander-Clark, A. R. C., and
1120 Becchio, R., 2020, Decoupled U-Pb date and chemical zonation of monazite in migmatites:
1121 The case for disturbance of isotopic systematics by coupled dissolution-precipitation:
1122 *Geochimica et Cosmochimica Acta*, v. 269, p. 398-412.
- 1123 Whitney, D. L., and Evans, B. W., 2010, Abbreviations for names of rock-forming minerals: *American*
1124 *Mineralogist*, v. 95, p. 185-187.
- 1125 Wilson, C. J. L., Russell-Head, D. S., Kunze, K., and Viola, G., 2007, The analysis of quartz c-axis fabrics
1126 using a modified optical microscope: *Journal of Microscopy*, v. 227, p. 30-41.
- 1127 Wing, B. A., Ferry, J. M., and Harrison, T. M., 2003, Prograde destruction and formation of monazite
1128 and allanite during contact and regional metamorphism of pelites: *Petrology and*
1129 *geochronology: Contributions to Mineralogy and Petrology*, v. 145, p. 228-250.

- 1130 Wolfram, L. C., Weinberg, R. F., Hasalová, P., and Becchio, R., 2017, How melt segregation affects
1131 granite chemistry: Migmatites from the Sierra de Quilmes, NW Argentina: *Journal of*
1132 *Petrology*, v. 58, p. 2339-2364.
- 1133 Wolfram, L. C., Weinberg, R. F., Nebel, O., Hamza, K., Hasalová, P., Míková, J., and Becchio, R., 2019,
1134 A 60-Myr record of continental back-arc differentiation through cyclic melting: *Nature*
1135 *Geoscience*, v. 12, p. 215-219.